

Modeling gas flow velocities in soils induced by variations in surface pressure, heat and moisture dynamics

W J Massman¹ and J M Frank¹

¹USDA Forest Service

November 23, 2022

Abstract

Changes in atmospheric pressure continuously ventilate soils and snowpacks. This physical process, known as pressure pumping, is a major factor in the exchange fluxes of H₂O, CO₂ and other trace gases between the soil and atmosphere. Thus models of pressure pumping are relevant to many areas of critical importance. This study compares the three principal models used to describe pressure pumping. Beginning with the fundamental physical principles and whether the flow field is compressible or incompressible, these models are categorized as linear parabolic (one model – compressible) or nonlinear hyperbolic (two models – incompressible). Using observed soil surface pressure data, measured vertical profiles of soil permeability and standard linear analysis and numerical methods, this study shows that nonlinear models produce advective velocities that are one to two orders of magnitude greater than those associated with the linear model. Incorporating soil temperature and moisture dynamics made very little difference to the linear model, but a significant difference in the nonlinear models suggesting that advective velocities induced by pressure changes associated with soil heating and moisture dynamics may not always be small enough to ignore. All numerical results are sensitive to the frequency of the pressure forcing, which was band-pass filtered into low, mid and high frequencies with the greatest model differences at low frequencies. Partitioning the pressure forcing and model responses helped to establish that mid-frequency weather-related phenomena (empirically identified as inertia gravity waves and solitons) are important drivers of gas exchange between the soil and the atmosphere.

Abstract

Changes in atmospheric pressure continuously ventilate soils and snowpacks. This physical process, known as pressure pumping, is a major factor in the exchange fluxes of H_2O , CO_2 and other trace gases between the soil and atmosphere. Thus models of pressure pumping are relevant to many areas of critical importance. This study compares the three principal models used to describe pressure pumping. Beginning with the fundamental physical principles and whether the flow field is compressible or incompressible, these models are categorized as linear parabolic (one model – compressible) or nonlinear hyperbolic (two models – incompressible). Using observed soil surface pressure data, measured vertical profiles of soil permeability and standard linear analysis and numerical methods, this study shows that nonlinear models produce advective velocities that are one to two orders of magnitude greater than those associated with the linear model. Incorporating soil temperature and moisture dynamics made very little difference to the linear model, but a significant difference in the nonlinear models suggesting that advective velocities induced by pressure changes associated with soil heating and moisture dynamics may not always be small enough to ignore. All numerical results are sensitive to the frequency of the pressure forcing, which was band-pass filtered into low, mid and high frequencies with the greatest model differences at low frequencies. Partitioning the pressure forcing and model responses helped to establish that mid-frequency weather-related phenomena (empirically identified as inertia gravity waves and solitons) are important drivers of gas exchange between the soil and the atmosphere.

Plain Language Summary

Atmospheric pressure is constantly moving air in, out and through the surface of the soil or a snowpack. This pressure pumping (or ventilating) mechanism influences soil water evaporation and snow sublimation, the fluxes of key climate-warming greenhouse gases, and rate at which contaminants can be removed from soils. Thus the ability to model the movement of these gases through these two media is relevant to many current environmental concerns. The present study discusses the differences between the two broad categories of pressure pumping models and points out that these models predict very different ventilation rates. So different that it may be possible to conclude (incorrectly) that the daily cycle for pressure is not significant to soil or snowpack gas exchange. These two model types also respond differently when pressure changes are influenced by changes in soil temperature and moisture, with one type suggesting that dynamic soil temperature and moisture effects are small, in agreement with expectations, and the other suggesting that they can cause surprisingly large effects. Present results also identify (for the first time) specific meso-scale atmospheric waves, often associated with frontal systems, convective activity and rain, can be significant drivers of pressure induced gas exchange.

1 Introduction

For nearly the past 120 years variations in atmospheric pressure and wind at the earth's (solid) surface have been understood as a key mechanism responsible for air movement in and out of soils (Buckingham, 1904) and snowpacks (Dubrovin, 1961). For nearly as long variations of these atmospheric variables have formed the basis for modeling the induced advective velocities within soils (Buckingham, 1904) and snowpacks (Clarke et al., 1987). This phenomenon is often identified as “pressure pumping”, “barometric pumping” or “windpumping”. (Note: The term pressure pumping will be used exclusively in the present study.) Thus this study focuses advective currents in soils that are driven by periodic (mechanically forced or thermally induced) pressure variations that are distinct from density or thermally driven (i.e., overturning) convective currents that often

63 dominate fractured or high permeability soils (e.g., Falta et al. (1989); Weisbrod et al.
64 (2009); Nachshon et al. (2012))

65 Understanding and modeling this phenomenon are important because such air cur-
66 rents can influence key physical and biological processes in the soil and snowpacks through
67 their ability to modify concentration profiles and advective fluxes of gases within and
68 through the pore spaces of these permeable media. For example, these air current trans-
69 port O₂ (Scotter et al. (1967); Elberling et al. (1998)), CO₂ through both soils (Lewicki
70 et al. (2003); Reicosky et al. (2008); Maier et al. (2012); Laemmel et al. (2017); Moya
71 et al. (2019)) and snowpacks (Bowling and Massman (2011); Berryman et al. (2018);
72 and the video postcard Massman et al. (2021)), water vapor (Fukuda (1955); Scotter and
73 Raats (1969)), CH₄ (Shurpali et al. (1993); Czepiel et al. (2003); Xu et al. (2014); Forde
74 et al. (2019)), N₂O (Massman et al., 1997), gaseous radioactive contaminants (Bourret
75 et al., 2018), Hg vapor (Faïn et al., 2013), isotopes of Rn (Clements and Wilkening (1974);
76 Chen et al. (1995); Robinson et al. (1997); Hu et al. (2018)) and He (Hinkle, 1994). Fur-
77 thermore, this transport mechanism influences the rate of evaporation of soil water (Ishi-
78 hara et al., 1992), the sublimation rate of snowpacks (Albert (2002); Drake et al. (2019)),
79 and the volatilization rates and fate of soil contaminants, such as jet fuel (Ostendorf et
80 al., 2000) or other soil contaminants (Forde et al., 2019). In addition, knowledge of the
81 advective velocities induced by pressure pumping may help improve the long term mea-
82 surements of ecosystem CO₂ fluxes and carbon balance (Massman & Lee, 2002), the for-
83 mulation of the soil surface boundary condition for land surface (soil-plant-atmosphere)
84 models (e.g., Grifoll et al. (2005)), the fluxes of soil-generated greenhouse gases for cli-
85 mate studies (e.g., Todd-Brown et al. (2012); Rains et al. (2016)), and the transport and
86 deposition of combustion products into the soil during prescribed fires (Massman et al.,
87 2010). The fact that pressure pumping is an important and significant mode of the ex-
88 change between the vadose zone and the atmosphere (e.g., Etiope and Martinelli (2002);
89 Rutten (2015)) leads directly to one of the intentions of the present study, which is to
90 expand the research horizons in the area. Nevertheless, this is not necessarily straight-
91 forward for three reasons.

92 First, there are three models describing pressure pumping. The principal difference
93 between them arises when assuming that the flow field is either compressible or incom-
94 pressible, which in turn leads to estimates of the vertical advective velocity at the soil
95 surface that differ by one or more orders of magnitude, even with identical forcing and
96 soil structure. This difference is significant enough that pointing it out and quantifying
97 it as much as possible is the first intention of the present study. The range and number
98 of settings for interactions between the atmosphere and the earth’s surface that involve
99 pressure pumping (e.g., Kuang et al. (2013)) more than justifies a careful look at the dif-
100 ferences between these three models.

101 Second, beyond the mechanical forcing of soil by fluctuations in atmospheric pres-
102 sure at the soil surface, surface heating can force temperature variations within perme-
103 able media and thereby also induce advective flows in both soil (e.g., Kimball (1983); Hin-
104 kle (1994); Parlange et al. (1998); Novak (2016)) and snowpacks (e.g., Gray and Mor-
105 land (1994); Massman et al. (1997); Bartelt et al. (2004)). This is easily understood from
106 the ideal gas law. Whenever the gas temperature within the gas-filled portion of a pore
107 volume changes so also must the pore air pressure (i.e., $\partial p/\partial t \propto \partial T/\partial t$, assuming that
108 the gas filled pore volume is constant), which by Darcy’s law will produce an advective
109 flow. But within soils the gas-filled pore volume can change whenever soil water changes
110 phase, i.e., during evaporation or condensation, and during rainfall or irrigation and the
111 concomitant movement of water through the soil matrix. These temperature and mois-
112 ture influences on induced advective flows have been considered by a few authors, e.g.,
113 Kimball (1983); Parlange et al. (1998); Jury and Horton (2004) and Novak (2016) all
114 explore possible temperature effects and Lebeau and Konrad (2009) include the possi-
115 bility of dynamic changes in soil moisture as part of their modeling study. But it is ex-

pected that temperature and moisture effects are likely to be very small compared to direct pressure effects e.g., Kimball (1983); Massman et al. (1997); Novak (2016)). Nonetheless, (Jury & Horton, 2004, p. 207) do suggest that “Thermally induced convection [authors: ‘advection’] is a topic in need of further evaluation”, which is the second intent of the present study.

Third, atmospheric pressure at the earth’s surface is extraordinarily dynamic and complex, occurring on a variety of scales ranging from weather related high and low pressure systems (the low frequency synoptic scale), through the daily and sub-daily cycles caused by tidal forces and the shorter and more localized mesoscale events (thunderstorms, squall lines, downslope windstorms) to the scale of turbulence (with a time scale on the order of 1-100 seconds or so and a spatial scale of a meter or so). Although these meteorological phenomena are easily identified and often have well characterized barometric pressure signals associated with them, any observed pressure signal will also include common phenomena, which to the authors’ knowledge have not been discussed in relation to their forcing of advective flows in soils. Such phenomena include atmospheric infrasound (e.g., Bedard (1998, 2005); Leventhall (2007); Raspert et al. (2019)), high frequency gravity waves (e.g., Marlton et al. (2019); X. Wang et al. (2020)) and other high frequency atmospheric coherent structures (e.g., Einaudi et al. (1989)), lower frequency inertia-gravity waves and other mesoscale scale gravity waves (e.g., Grivet-Talocia et al. (1999); Koch and Siedlarz (1999); Ralph et al. (1999); Koppel et al. (2000); Ruppert and Bosart (2014)), density currents, atmospheric bores and solitons or solitary waves (e.g., Shreffler and Binkowski (1981); Goncharov and Matveyev (1982); Doviak and Ge (1984); Christie (1989); Hauf et al. (1996)). Finally, any measured soil surface pressure signal could also include components unique to a specific location when wind interacts with vegetation (e.g., Finnigan (1979); Shaw et al. (1990); H. Wang and Takle (1995); Nieveen et al. (2001)). The final purpose of the present study is to point out that (what appear in the data to be) inertia-gravity waves and solitons can induce significant advective flows in soils.

The remainder of this study consists four sections. The following section outlines the basic physical and modeling fundamentals and includes an order of magnitude calculation for the advective velocities associated with the different physical processes and models. This second section also develops a semi-observationally based approach for estimating advective velocities in-situ in the hope of better understanding the differences in modeled advective velocities. The third section discusses the experimental site, Manitou Experimental Forest or MEF, and the associated pressure and soil data used with the models. The fourth section presents the results and discussion in terms of three frequency bands for the pressure forcing. Filtering the pressure signal into low (periods ≥ 5 hours), mid (periods between 0.5 and 5 hours) and high (periods ≤ 0.5 hrs) frequencies helps illuminate the significance impact that inertia-gravity waves and solitons (or more generally, organized mid frequency atmospheric phenomena) can have on pressure pumping in soils. The final section is the summary and conclusion.

2 Physical Fundamentals of Pressure Pumping

Darcy’s law and the conservation of mass of soil air (or the equation of continuity of pore air) are foundational elements to developing a model of induced advective flows in soils (e.g., Muskat (1937); Nield (1982); Phillips (1991); Scanlon et al. (2002); Novak (2016)). The 3-D versions of Darcy’s law and the conservation of mass (in order) are

$$(\eta - \theta)\mathbf{v} = -\frac{k}{\mu}\nabla P_a \quad (1)$$

and

$$\frac{\partial((\eta - \theta)\varrho_a)}{\partial t} + \nabla \bullet (\mathbf{J}_a + (\eta - \theta)\varrho_a \mathbf{v}) = S_a \quad (2)$$

where bold variables are 3-D vectors and \mathbf{v} (ms^{-1}) is the velocity field within the soil, k (m^2) is the soil permeability, μ (Pa s) is the dynamic viscosity of soil air, ∇ (m^{-1}) is the spatial gradient operator, P_a (Pa) is the soil air pressure, η (m^3m^{-3}) is total soil porosity, θ (m^3m^{-3}) is the soil volumetric moisture content, $(\eta - \theta)$ is, therefore, the air-filled porosity, ϱ_a (mol m^{-3}) is the molar density of the soil air, t (s) is time, \mathbf{J}_a ($\text{mol m}^{-2}\text{s}^{-1}$) is the diffusional flux of air entering and exiting a soil pore, and S_a ($\text{mol m}^{-3}\text{s}^{-1}$) is the source/sink term of the production/destruction of pore air within the soil.

Because the focus here is on the primary mechanisms causing advective flows the molar diffusive flux, \mathbf{J}_a , will not be considered. Further, the source term, S_a , can be eliminated from Equation (2) without sacrificing the influence that changes in θ can have on \mathbf{v} (e.g., Parlange et al. (1998); Lebeau and Konrad (2009); Novak (2016)). In the present context, S_a would only be used to describe soil biochemical reactions involving soil CO_2 , O_2 and various nitrogen species, which would have virtually no effect on the air-filled pore volume or \mathbf{v} . After these simplifications the ideal gas law is combined with Equation (2); where the ideal gas law is $P_a = \varrho_a R T_K$ and $R = 8.314 \text{ Jmol}^{-1}\text{K}^{-1}$ is the universal gas constant and T_K (K) is the temperature of both the soil air and the soil matrix, which are assumed to be in thermal equilibrium. The resulting equation forms the basis for two different, but related, purposes. The first is prognostic model development (including an order of magnitude estimate of the terms appearing in the various models) and the second is model diagnostics (i.e., model comparisons). Each of these approaches is taken in turn.

2.1 Prognostic Models and Modeling Methods

For prognostic modeling purposes the following equation follows from employing the ideal gas law with Equation (2)

$$\frac{\partial P_a}{\partial t} + \mathbf{v} \bullet \nabla P_a + P_a \nabla \bullet \mathbf{v} = \frac{P_a}{T_K} \left(\frac{\partial T_K}{\partial t} + \mathbf{v} \bullet \nabla T_K \right) + \frac{P_a}{(\eta - \theta)} \left(\frac{\partial \theta}{\partial t} + \mathbf{v} \bullet \nabla \theta \right) \quad (3)$$

Further model development requires simplifying this last expression to 1-D (vertical only), but first it is important to comment on the compressible flow term, $P_a \nabla \bullet \mathbf{v}$, because assuming that the flow is compressible ($\nabla \bullet \mathbf{v} \neq 0$) leads to a very different model of pressure pumping than assuming that the flow is incompressible ($\nabla \bullet \mathbf{v} = 0$).

Many pressure pumping models assume incompressible flow (e.g., Muskat (1937); Albert and McGilvary (1992)), as do models of atmospheric pressure fluctuations at the soil surface (e.g., Kraichnan (1956); Yu et al. (2011)), which eliminates the compressible flow term a priori. This is reasonable because in the absence of shocks compressible flow effects are negligible. Or, stated more precisely, compressible flow effects only become important for Mach numbers > 0.3 (Depcik & Loya, 2012), which is not physically realistic for velocities associated with induced advective flows in soils or snowpacks. On the other hand it is appropriate to keep the compressible flow term when describing propagation of sound through soil (e.g., Phillips (1991)). But it is unclear (at least to these authors) how pressure fluctuations associated with sound waves can have any significant influence on advective motions in soils. Nonetheless, the compressible flow model has been used to describe pressure pumping effects (e.g., Buckingham (1904); Clarke et al. (1987)) so it is appropriate to include in this study.

Decomposing the forcing variables (P_a , T_K , θ) into temporally and spatially invariant background components and components that vary with time and spatial dimension, the 1-D form of Equation (3) is

$$\frac{\partial p_\beta}{\partial t} + v \frac{\partial p_\beta}{\partial z} + (P + p_\beta) \frac{\partial v}{\partial z} = \frac{P}{T_K} \left(\frac{\partial T_\beta}{\partial t} + v \frac{\partial T_\beta}{\partial z} \right) + \frac{P}{(\eta - \theta)} \left(\frac{\partial \theta_\beta}{\partial t} + v \frac{\partial \theta_\beta}{\partial z} \right) \quad (4)$$

where z (m) is the soil depth, v is the induced advective velocity in the vertical direction, the β -subscripted variables ($p_\beta = p_\beta(z, t)$ (Pa); $T_\beta = T_\beta(z, t)$ (C); $\theta_\beta = \theta_\beta(z, t)$ (m^3m^{-3})) are the temporally and spatially varying components of P_a , T_K and θ , and P is the time and spatially invariant component of P_a (i.e., $P_a = P + p_\beta$). In general $P \gg p_\beta$ so P substitutes for P_a on the right hand side of Equation (4). But not so on the left hand side because the term $p_\beta \partial v / \partial z$, although relatively small, is relevant and important to the approximate model of pressure pumping in soils discussed below. Also note that the temporally and spatially invariant background components of T_K and θ are not explicitly used as modeling variables.

2.1.1 Three models of advective flows: Pressure forcing only

Traditionally “pressure pumping” models ignore the temperature and soil moisture terms on the right hand side of Equation (4). Including the T_K and θ terms in the three models developed in this section is deferred until the next section, section 2.1.2.

The first model of pressure-only induced advective flows discussed in this section is the Linear (Buckingham, 1904, Appendix A), or Compressible Flow model, the full expression of which follows immediately from Equation (4) and is given as

$$\frac{\partial p_\beta}{\partial t} + v \frac{\partial p_\beta}{\partial z} + (P + p_\beta) \frac{\partial v}{\partial z} = 0 \quad (5)$$

or when combined with Darcy’s law is

$$\frac{\partial p_\beta}{\partial t} - \frac{\partial}{\partial z} \left(\kappa \frac{\partial p_\beta}{\partial z} \right) - \frac{\kappa}{P} \left(\frac{\partial p_\beta}{\partial z} \right)^2 - \frac{p_\beta}{P} \frac{\partial}{\partial z} \left(\kappa \frac{\partial p_\beta}{\partial z} \right) = 0 \quad (6)$$

where $\kappa = Pk / ((\eta - \theta)\mu)$ (m^2s^{-1}) is the “pressure diffusivity” (and Darcy’s Law is expressed as $v = -(\kappa/P) \partial p_\beta / \partial z$). The difference between this last expression and Buckingham’s original model is that his model includes only the first term on the left hand side and not the second or third terms, both of which are quite small relative to first term. It is easy to see that the third term on the left can be ignored relative to the first, because it follows immediately from $p_\beta \ll P$ or equivalently $p_\beta/P \ll 1$. Showing that the second term on the left is small relative to the first term, i.e., $\kappa/P (\partial p_\beta / \partial z)^2 \ll \partial / \partial z (\kappa \partial p_\beta / \partial z)$ is somewhat more involved and so is left for Section 2.2.1. Therefore, the Linear model (Buckingham, 1904), which is given next, should be accurate to a high degree of numerical precision.

$$\frac{\partial p_\beta}{\partial t} - \frac{\partial}{\partial z} \left(\kappa \frac{\partial p_\beta}{\partial z} \right) = 0 \quad \text{Linear model} \quad (7)$$

Before proceeding to the second model there is an interesting variant to Buckingham’s original model, which is

$$\frac{\partial p_\beta}{\partial t} - \frac{\partial}{\partial z} \left(\kappa \frac{\partial p_\beta}{\partial z} \right) - \frac{\kappa}{P} \left(\frac{\partial p_\beta}{\partial z} \right)^2 = 0 \quad (8)$$

which follows by dropping the third term of Equation (6) (because as shown in section 2.1.2, $(p_\beta/P) \partial/\partial z (\kappa \partial p_\beta/\partial z) \ll \kappa/P (\partial p_\beta/\partial z)^2$). Unlike Buckingham's original model, which is linear and parabolic, this equation is weakly non-linear, although still parabolic because as discussed above the first term on the right is still much larger than the non-linear second term. This variant of the Linear pressure pumping model is pointed here because, as shown in the Appendix A, Equation (8) can be related to the viscous Burgers Equation and is, therefore, amenable to an analytical solution.

The second model explored here is the Muskat (Muskat, 1937) or Incompressible Flow model, which is given as

$$\frac{\partial p_\beta}{\partial t} + v \frac{\partial p_\beta}{\partial z} = 0 \quad (9)$$

When combined with Darcy's law this yields:

$$\frac{\partial p_\beta}{\partial t} - \frac{k}{(\eta - \theta)\mu} \left(\frac{\partial p_\beta}{\partial z} \right)^2 = 0 \quad \text{or} \quad \frac{\partial p_\beta}{\partial t} - \frac{\kappa}{P} \left(\frac{\partial p_\beta}{\partial z} \right)^2 = 0 \quad \text{Muskat model} \quad (10)$$

where the compressible flow term (which is proportional to $\partial v/\partial z$) does not appear in this model. Unlike the Linear model, this model is nonlinear and hyperbolic and, as also shown in Appendix A, can be transformed into the inviscid Burgers Equation. Although this identity with the Burgers Equation is not employed in this study, it is worth pointing out because this may offer other insights into solution methods for Equation (10).

The third model of pressure pumping is an approximation to the Muskat model that originated with Kidder (1957) (crediting Muskat (1937)) and further developed by J. W. Massmann (1989). It is obtained by adding $-(\kappa/P) p_\beta (\partial^2 p_\beta/\partial z^2)$ to the left hand side (of the second expression) of Equation (10) and then employing the identity $(\partial p_\beta/\partial z)^2 + p_\beta (\partial^2 p_\beta/\partial z^2) = \partial^2(p_\beta^2/2)/\partial z^2$ to yield the Kidder model, or the Approximate Incompressible Flow model:

$$\frac{\partial p_\beta}{\partial t} - \left(\frac{\kappa}{P} \right) \frac{\partial^2(p_\beta^2/2)}{\partial z^2} = 0 \quad \text{Approximate model} \quad (11)$$

This model is only justifiable because the term, $p_\beta (\partial^2 p_\beta/\partial z^2)$ is quite small relative to the original nonlinear term, $(\partial p_\beta/\partial z)^2$, an inequality that was discussed above and is proven in section 2.2.1. Although the Kidder model may appear to be a nonlinear parabolic equation, it remains a nonlinear hyperbolic equation. Interestingly though, the Approximate model may offer some computational benefit over the Muskat model because it was often more stable numerically than the Muskat model – likely because of the addition of a weak, albeit non-linear, diffusive term (e.g., Thomas (1995, Section 5.3.3)).

In summary, the three models examined in this study are Equation (7) (the Linear or Compressible Flow model), Equation (10) (the Muskat or Incompressible Flow model) and Equation (11) (the Kidder or the Approximate Incompressible Flow model) and, as demonstrated in Section 4, there are some significant differences in the predictions of $v(t, z)$

and (especially) $v(t, 0)$ that are associated with these three models. But before ending this section, it may be worth a brief discussion of the model first proposed by Shan (1995) and further developed by Scanlon et al. (2002) and later employed by J. Li et al. (2011) and (especially) J. Li et al. (2012).

The Quasi-Linear model (Shan (1995); Scanlon et al. (2002)) is

$$\frac{\partial P_a^2}{\partial t} - \kappa \frac{\partial^2 P_a^2}{\partial z^2} = 0 \quad \text{Quasi-Linear model} \quad (12)$$

Except for a change of notation this last equation is identical to Equation (1) of Shan (1995) and Equation (8.30) of Scanlon et al. (2002). But Scanlon et al. (2002) show that the Quasi-linear model can be linearized to yield what is essentially the Compressible Flow model, Equation (7) above (see Equation (8.31) of Scanlon et al. (2002)). But the Compressible Flow model can only be derived by assuming the flow is compressible. It is by its nature predominantly linear (as shown previously) and it is not a consequence of the linearization of a nonlinear model. Therefore, the Quasi-Linear model is completely unnecessary. But more importantly, combining either Equation (8.30) of Scanlon et al. (2002) or equivalently Equation (12) with the incompressible flow assumption does not and cannot logically lead to Equation (8.31) of Scanlon et al. (2002) (= the Compressible Flow model). Therefore, models based on the Quasi-Linear model, Equation (12) above, are at the very least unnecessary and may in fact be completely wrong, especially if it is thought of as a further refinement of the Approximate Incompressible Flow model (Equation (11) above). Confusing Equation (12) as a variant of Equation (11) might lead to substituting p_β for P_a in Equation (12) above (i.e., replacing Equation (12) with $\partial p_\beta^2 / \partial t - \kappa \partial^2 p_\beta^2 / \partial z^2 = 0$). This last equation for p_β^2 cannot be logically justified on the basis of being related to the Approximate model. Regardless of the assumption made concerning the flow, simply recognizing that the Approximate model is valid is sufficient to show that the equation $\partial p_\beta^2 / \partial t - \kappa \partial^2 p_\beta^2 / \partial z^2 = 0$ violates the physically valid assumption that $p_\beta \ll P$.

2.1.2 Three models of advective flows: Including T_K and θ forcing

Each of the three models discussed above can be generalized to include the influence that changes in soil temperature and moisture can have on $p_\beta = p_\beta(t, z)$ and $v = v(t, z)$. These generalizations are (in the order as above)

$$\frac{\partial p_\beta}{\partial t} - \frac{\partial}{\partial z} \left(\kappa \frac{\partial p_\beta}{\partial z} \right) + \Lambda_z \frac{\kappa}{P} \left(\frac{\partial p_\beta}{\partial z} \right) = \Lambda_t \quad \text{Linear model} \quad (13)$$

$$\frac{\partial p_\beta}{\partial t} - \frac{\kappa}{P} \left(\frac{\partial p_\beta}{\partial z} \right)^2 + \Lambda_z \frac{\kappa}{P} \left(\frac{\partial p_\beta}{\partial z} \right) = \Lambda_t \quad \text{Muskat model} \quad (14)$$

$$\frac{\partial p_\beta}{\partial t} - \frac{\kappa}{P} \left(\frac{\partial^2 (p_\beta^2 / 2)}{\partial z^2} \right) + \Lambda_z \frac{\kappa}{P} \left(\frac{\partial p_\beta}{\partial z} \right) = \Lambda_t \quad \text{Approximate model} \quad (15)$$

where Λ_t (Pa s^{-1}) = $\Lambda_t(t, z) = (P/T_K)\partial T_\beta/\partial t + (P/(\eta-\theta))\partial\theta_\beta/\partial t$ and Λ_z (Pa m^{-1}) = $\Lambda_z(t, z) = (P/T_K)\partial T_\beta/\partial z + (P/(\eta-\theta))\partial\theta_\beta/\partial z$.

To keep the modeling and numerical methods as simple and as realistic as possible $\Lambda_t(t, z)$ and $\Lambda_z(t, z)$ are input as external analytical expressions obtained by differentiating analytical expressions for $T_\beta(t, z)$ and $\theta_\beta(t, z)$, which are obtained by curve-

fitting the observed soil surface temperature, $T_\beta(t, 0)$, and the 0.02 m depth soil moisture, $\theta_\beta(t, z = 0.02 \text{ m})$. Here I assume that $\theta_\beta(t, 0) \approx \theta_\beta(t, z = 0.02 \text{ m})$, which is not unreasonable for the present study because it is focused on a very dry semiarid site that does not display strong moisture dynamics.

$T_\beta(t, 0)$ is approximated analytically as $\Sigma_i F_{Ti}(t, 0)$, where $F_{Ti}(t, 0) = \Delta T_{\beta i} \sin(\omega_i t + \phi_i)$ is the predominant functional form, but can be other functions necessary to capture low and mid-frequency transients associated with synoptic scale weather systems or clouds. Given an analytical expression for $T_\beta(t, 0)$, then $T_\beta(t, z) = \Sigma_i F_{Ti}(t, z) \exp(-z/D_{Ti})$, where $F_{Ti}(t, z) = \Delta T_{\beta i} \sin(\omega_i t + \phi_i - z/D_{Ti})$ and D_{Ti} is estimated by scaling the temperature attenuation depth associated with the diel cycle, D_T (where D_T was determined from the observed temperature profiles to be 0.12 m during June 2012 and 0.14 m during October 2012), to ω_i (or other non-sinusoidal frequency-like parameters). The sampling frequency for the soil surface temperature (5 minutes) and the sensitivity of the soil temperature probe largely eliminated any possibility of obtaining any high frequency temperature data information for the present study. Consequently, the only frequency content in the temperature data are the low and mid frequencies.

A similar method is employed for the soil moisture at 0.02 m, i.e., $\theta_\beta(t, z = 0.02 \text{ m}) = \Sigma_i F_{\theta i}(t, 0)$. The set of functions $F_{\theta i}(t, 0)$ are largely specific to a given observation period and are not necessarily sinusoidal in time to allow for those occasions when rain may rapidly increase soil moisture or the soil moisture decreases with drying or drainage. The attenuation depths for soil moisture variations were modeled in a manner similar to temperature, but inferred from the moisture observations. But precision estimates in the attenuation depths for soil moisture are not critical to the model simulations because the soil was extremely dry during the observation periods and most soil moisture dynamics were confined to the upper few centimeters of soil, except for the overall drying trend in soil moisture, which did extend to nearly a meter in depth. But because of the nature of the data and the sensitivity of the soil moisture probe $\theta_\beta(t, z)$ contains only low frequency information. Finally, because soil moisture at this site was generally less than $0.15 \text{ m}^3 \text{ m}^{-3}$ at all times there is no concern about a saturated soil, i.e., $(\eta - \theta) \rightarrow 0$ in the denominator of either $\Lambda_t(t, z)$ and $\Lambda_z(t, z)$.

The initial conditions for temperature and moisture, $T_K(0, z)$ and $\theta(0, z)$, are obtained by curve fitting their observed profiles at the start of the simulation.

2.1.3 Numerical methods, Initial conditions and Boundary conditions

The Linear models, Equations (7) and (13), are solved numerically using an implicit Crank-Nicolson scheme followed by three iterations of a Newton-Raphson solver to refine the Crank-Nicolson solution. Three iterations of the Newton-Raphson solver were sufficient to produce a convergence $< 10^{-10}$ Pa. The nonlinear models, Equations (10) and (14) for the Muskat model and Equations (11) and (15) for the Approximate model, are solved with an implicit finite difference scheme adapted after Lax-Friedrichs method (e.g., Thomas (1995, p. 215); Press et al. (2007, p. 1034); Kurganov (2016, Eqn. (26)); Hinch (2020, Chapter 10)), which is followed by three iterations of the Newton-Raphson solver again achieving a convergence $< 10^{-10}$ Pa. The Newton-Raphson step is intended to reduce numerical errors in the solution for $p_\beta(t, z)$ and thereby improve stability of the Lax-Friedrichs scheme for the hyperbolic models. It was of less benefit to the Crank-Nicolson scheme and the Linear models.

But because the nonlinear hyperbolic models discussed here, i.e, Equations (10) and (11), do not quite fit the archetypal Lax-Friedrichs schemes discussed in the references above it is worthwhile to briefly discuss the numerical method used here. The most fundamental expression of which is the following:

$$\tilde{p}_i^{j+1} - \left(\frac{\Delta t}{4\Delta z^2} \frac{\kappa_i}{P} \right) (\tilde{p}_{i+1}^{j+1} - \tilde{p}_{i-1}^{j+1})^2 = \frac{1}{2} (\tilde{p}_{i+1}^j + \tilde{p}_{i-1}^j)$$

375 where $i = 1, 2, \dots, M$ refers to the spatial discretization index (with M layers) and j
 376 is the time step index. In terms of the Newton-Raphson function to be minimized at the
 377 $j + 1$ time step, i.e., $\tilde{P}_i = \tilde{P}_i(\tilde{p}_{i-1}^{j+1}, \tilde{p}_i^{j+1}, \tilde{p}_{i+1}^{j+1})$, this yields:

$$\tilde{P}_i = \tilde{p}_i^{j+1} - \frac{r_i}{4} (\tilde{p}_{i+1}^{j+1} - \tilde{p}_{i-1}^{j+1})^2 - \frac{1}{2} (\tilde{p}_{i+1}^j + \tilde{p}_{i-1}^j)$$

378 where $r_i = \Delta t \kappa_i / (\Delta z^2 P)$ (Pa^{-1}) and this numerical scheme, appropriate to the Muskat
 379 model, is easily generalized to the Approximate model and the models that include tem-
 380 perature and moisture dynamics. Although this Lax-Friedrichs-Newton-Raphson numer-
 381 ical scheme does appear to yield quite plausible and physically realistic solutions, it was
 382 not the only numerical scheme investigated. The explicit Lax-Friedrichs method and both
 383 the explicit and implicit Lax-Wendroth (with a Newton-Raphson solver for the implicit
 384 approach) were also investigated and compared. The present scheme seems to be the most
 385 reliable of all those tested. Possible contributing factors to the performance of the present
 386 numerical scheme is that the velocity field being modeled is unlikely to develop shocks,
 387 nor are there any discontinuities in the input data that are sufficient to promote their
 388 formation.

389 The initial condition for pressure cannot be determined directly from observations.
 390 Therefore, the present study assumes that $p_\beta(0, z) = p_\beta(0, 0)(1 - \epsilon + \epsilon \exp(-z/D_{p,init}))$,
 391 where $p_\beta(0, 0)$ is the observed surface pressure perturbation at $t = 0$, $\epsilon = 0.08$ and
 392 $D_{p,init} = 60$ m. This parameterization is somewhat arbitrary, but it is reasonable and
 393 it provides a simple continuous function for the model's initial conditions. Furthermore,
 394 since the purpose of the present study is to compare different model estimates of $v(t, z)$
 395 and especially $v(t, 0)$ the key consideration here is not whether the models are sensitive
 396 to the initial conditions, but that the initial conditions are the same for each model run.
 397 Nonetheless, a sensitivity analysis was performed to examine the model's sensitivity to
 398 ϵ and $D_{p,init}$ by first comparing $\epsilon = 0$ (uniform initial pressure field) with that assum-
 399 ing $\epsilon = 0.08$. The difference in the Linear and Muskat model all frequencies solutions
 400 near the surface, $v(t, 0)$, were usually quite small $< 0.1\%$. The differences could be larger
 401 at greater depths because the permeability at this site increases by a couple orders of
 402 magnitude within the upper 0.5 m of soil, but again not significantly so. Similar con-
 403 clusions were reached when varying $D_{p,init}$, except for the Muskat model for low frequen-
 404 cies, for which the difference was $< 6\%$. In general, the initial conditions should not be
 405 viewed as a source of significant concern in the preset study.

406 The lower bound of the spatial domain is 20 m (below the soil surface) and the grid
 407 spacing is 0.10 m for all models. The lower boundary condition (LBC) is $\partial^2 p_\beta / \partial z^2 =$
 408 0, i.e., a "pass-through" boundary condition. But because the soil permeability was set
 409 to a very low value ($k \leq 10^{-15} \text{ m}^2$) in the lowest third of the domain (a region of the
 410 soil for which there is no permeability data), the solution is not very sensitive to the specifics
 411 of the LBC. This constraint on k also helped improve stability of the numerical solution
 412 of the nonlinear models. The upper boundary condition is obtained from differential pres-
 413 sure measurements made on the soil surface and sampled at once per second (1 Hz). The
 414 1 Hz pressure time series was decomposed using a Savitzky-Golay filter (e.g., Press et
 415 al. (2007, p. 766)) into a low frequency component (pressure signals with periods ≥ 5
 416 hours), a mid-range frequency component (pressure signals with periods between 0.5 and
 417 5 hours) and high frequency component (with periods between 1 s and 0.5 hours). Each
 418 of these component time series is used separately for the upper boundary condition. To
 419 minimize potential numerical instabilities, particularly for the Muskat model, the time
 420 step is set to 1 second, i.e., the upper boundary condition is the observed or filtered 1

421 Hz pressure data. Likewise, the analytical expressions for $\Lambda_t(t, z)$ and $\Lambda_r(t, z)$ are in-
 422 put at 1 second intervals. All model coding was done in MatLab version 2019b.

423 2.2 Preliminary Model Diagnostics

424 2.2.1 A Numerical Example: Advective Velocities and Soil Evaporation

425 Because much of this study is devoted to comparing magnitudes of different esti-
 426 mates of the advective velocity this section provides some context for these estimates us-
 427 ing soil evaporation as an example. But, it is also important to emphasize that soil evap-
 428 oration is just one of many possible examples, so this particular case is not necessarily
 429 indicative of the significance of advective transport of any other trace gas in soil or other
 430 permeable media or for other environmental settings.

431 The advective flux of water vapor from the soil is $\rho_v v$ ($\text{kgm}^{-2}\text{s}^{-1}$), where ρ_v (kgm^{-3})
 432 is the mass density of the advected soil vapor and v (ms^{-1}) is the (vertical) advection
 433 velocity. To aid in the interpretation of the mass fluxes this evaporative flux is expressed
 434 in terms of energy units, i.e., the flux is $L_v \rho_v v$; where L_v is the enthalpy of vaporiza-
 435 tion of water $\approx 2.5 \times 10^6$ Jkg^{-1} . Assuming that the soil temperature is between 10 C
 436 and 30 C and that the soil vapor is saturated, it follows that ρ_v is between 0.01 and 0.03
 437 kgm^{-3} . Next allowing v to be between 1 and 1000 μms^{-1} (values that will be discussed
 438 and justified in the next and later sections), it follows that evaporative energy flux (den-
 439 sity) should be between about 0.025 Wm^{-2} and 75 Wm^{-2} . Or to put it another way,
 440 assuming any advective flux that contributes more than approximately 5 Wm^{-2} to soil
 441 evaporation is significant, then it follows that the advective velocity must exceed a thresh-
 442 old value of ≈ 100 μms^{-1} . For the present purposes, this threshold is fairly crude be-
 443 cause it can vary within a factor of two or so. But, it is not unreasonable and it should
 444 help with the interpretation of later results.

445 2.2.2 Linear Analysis: Magnitudes of advective velocities

446 This section serves two purposes. The first is to validate the expectations that
 447 $\kappa/P (\partial p_\beta/\partial z)^2 \ll \partial/\partial z (\kappa \partial p_\beta/\partial z)$ for the Linear model and $p_\beta (\partial^2 p_\beta/\partial z^2) \ll (\partial p_\beta/\partial z)^2$
 448 for the Approximate model. The second is to compare numerical estimates of the ad-
 449 vective velocities associated with each of the three pressure-only models to the temperature-
 450 only and θ -only models. For brevity and convenience this discussion is limited solely to
 451 the diel cycle (i.e., $\omega = 7.272 \times 10^{-5}$ radians s^{-1}). Nonetheless the numerical results
 452 (Section 4) validate the conclusions of this section for the diel cycle and show that the
 453 24-hour cycle is useful surrogate for all low frequencies (here defined with periods ≥ 5
 454 hours). The mid-range and high frequency results are deferred until Section 4 below, as
 455 are all results associated with including the temperature and θ effects (i.e., Equations
 456 (13), (14) and (15)).

457 The temperature-only advective velocity, v_T , is estimated from $\partial T_\beta/\partial t = v_T \partial T_\beta/\partial z$;
 458 where $\partial T_\beta/\partial t \approx \omega \Delta T_\beta$, $\partial T_\beta/\partial z \approx -\Delta T_\beta/D_T$, ΔT_β (C) is the amplitude of the diel
 459 cycle, D_T (m) is the attenuation depth associated with the diel-temperature wave, i.e.,
 460 $0.07 \text{ m} \leq D_T \leq 0.14 \text{ m}$ and for the sake of simplicity the phase between $\partial T_\beta/\partial t$ and
 461 $\partial T_\beta/\partial z$ is not considered in this section (which is the same for the pressure and soil mois-
 462 ture discussions below as well). Therefore,

$$|v_T| = \omega D_T \approx (5 - 10) \times 10^{-6} \text{ ms}^{-1}$$

463 where, because the principal concern here is orders of magnitude, the results are presented
 464 as absolute values (or equivalently the amplitude) of the induced advective velocities.
 465 Luce et al. (2013) use a similar approach to estimate the advective velocity of thermally

466 induced flow in stream beds. Also relevant here is the estimate of $|v_T|$ that can be de-
 467 rived from Kimball (1983), which is

$$|v_T| \approx (0.1) \times 10^{-6} \text{ ms}^{-1} \quad (\text{Kimball, 1983})$$

468 This is roughly two orders of magnitude smaller than the preceding estimate of v_T . This
 469 difference will be discussed further in Section 4.

470 The θ -only advective velocity, v_θ , is estimated from $\partial\theta/\partial t = v_\theta \partial\theta/\partial z$. But esti-
 471 mating $\partial\theta/\partial t$ and $\partial\theta/\partial z$ cannot be determined from a well established theory as was done
 472 with v_T . So both terms need to be estimated separately from observations. There are
 473 two components to $\partial\theta/\partial t$. The first is the amplitude of a daily cycle ($\Delta\theta_\beta$) and the other
 474 is a more-or-less decreasing linear trend. $\Delta\theta_\beta$ can be estimated from Rose (1968); R. D.
 475 Jackson (1973); T. J. Jackson et al. (1997); Brooks et al. (2002); Novak (2016) and the
 476 MEF data used in this study and presented later. This yields $\Delta\theta_\beta = 0.02 \text{ m}^3\text{m}^{-3}$ (vary-
 477 ing between 0 to $0.025 \text{ m}^3\text{m}^{-3}$), which suggests that $\omega\Delta\theta_\beta \approx 1.4 \times 10^{-6} \text{ s}^{-1}$. Novak
 478 (2016) estimates a maximum magnitude of the (decreasing) linear trend (i.e., a drying
 479 soil) to be θ to be $-1.2 \times 10^{-7} \text{ s}^{-1}$. The MEF data used in the present study suggest
 480 a similar value for a drying soil, but the same data also suggest that for a wetting soil
 481 $|\partial\theta/\partial t| > 1.4 \times 10^{-6} \text{ s}^{-1}$. Finally, the other data sources above suggest that for this
 482 decreasing linear trend $|\partial\theta/\partial t| < 10^{-8} \text{ s}^{-1}$ is also possible. Estimating a daily value of
 483 $\partial\theta/\partial z$ from these same data sources yields a value of $\partial\theta/\partial z$ of about 0.33 m^{-1} (varying
 484 between 0 to 0.4 m^{-1}). To keep the estimate of v_θ reasonable only $\partial\theta/\partial z = 0.33 \text{ m}^{-1}$
 485 is considered. Note that the data for some of these numerical estimates may not have
 486 included the temperature corrections appropriate to TDR measurements of volumetric
 487 soil moisture (e.g., Or and Wraith (2000); Massman et al. (2010, Appendix A)). We found
 488 that these corrections did not introduce any significant differences into the order of mag-
 489 nitude estimate of v_θ below or the conclusions drawn from them.

490 Synthesizing these results suggest

$$|v_\theta| = \frac{|\partial\theta/\partial t|}{|\partial\theta/\partial z|} \approx \frac{(0 - 1.6)10^{-6}}{0.33} \approx (0 - 5) \times 10^{-6} \text{ ms}^{-1}$$

491 This estimate of $|v_\theta|$, and especially the relatively larger values, are extremely uncertain
 492 (and potentially unreliable), largely because of the need to divide by $\partial\theta/\partial z$, which spans
 493 a very wide range including values approaching zero. The realism of the high end esti-
 494 mates of v_θ will be reexamined in Section 4.

495 Comparing these estimates of $|v_T|$ and $|v_\theta|$ suggest that $|v_\theta| < |v_T|$ is likely and,
 496 given the uncertainty inherent in v_θ , $|v_\theta| \ll |v_T|$ is nearly as likely. But in general when
 497 the soil is warming ($\partial T_\beta/\partial t > 0$) the soil dries out through evaporation, which results
 498 in $\partial\theta_\beta/\partial t < 0$. Therefore, v_θ will likely be (at least partially) out of phase with v_T and
 499 therefore, will reduce the effective v_T . So it is also reasonable to expect that $|v_\theta| < |v_T| +$
 500 $|v_\theta| \leq |v_T|$.

501 The pressure-only advective velocity is complicated by the need to examine three
 502 different models. For the Linear model to be valid it is necessary to show that the in-
 503 compressible term ($v_p \partial p_\beta / \partial z$) is much smaller than the compressible term ($P \partial v_p / \partial z$)
 504 for the following approximation to Equation (5) (i.e., $\partial p_\beta / \partial t = v_p \partial p_\beta / \partial z + P \partial v_p / \partial z$);
 505 where the ‘ p ’ subscript (v_p) refers to the pressure-induced velocity. Here I assume that
 506 both p_β and v_p attenuate with depth according to $\exp(-z/D_p)$, where D_p (m) is the pres-
 507 sure attenuation depth and that both are periodic in time, $\sin(\omega t)$. Therefore, analogous
 508 to T_β and v_T above, $\partial p_\beta / \partial t \sim \omega \Delta p_\beta$, $v_p \partial p_\beta / \partial z \sim v_p \Delta p_\beta / D_p$ and $P \partial v_p / \partial z \sim P v_p / D_p$;
 509 where Δp_β is the amplitude of the pressure “wave” at the soil surface. From $\Delta p_\beta \ll$
 510 P it follows that the incompressible term is much smaller than the compressible term

511 and the Linear model is valid. Therefore $v_{pL} = \omega D_p \Delta p_\beta / P$, where the ‘L’ subscript
 512 refers to ‘Linear model’. It is possible to estimate D_p from the linear theory of pressure
 513 pumping; i.e., $D_p = \sqrt{2\kappa/\omega}$ (e.g., Waddington et al. (1995)). Assuming a soil perme-
 514 ability (k) between 10^{-10} and 10^{-12} m², $\Delta p_\beta \sim 100$ Pa, $P = 10^5$ Pa, $\mu = 1.85 \times 10^{-5}$
 515 Pa s and $\eta - \theta \sim 0.4$, yields $\kappa = 0.0125 - 1.25$ m²s⁻¹, $D_p \sim 16 - 180$ m and the fol-
 516 lowing order of magnitude estimate of $|v_{pL}|$

$$|v_{pL}| = \omega D_p \frac{\Delta p_\beta}{P} = \left(\sqrt{2\kappa\omega}\right) \frac{\Delta p_\beta}{P} = (1 - 10) \times 10^{-6} \text{ ms}^{-1}$$

517 The range of values for $10^{-12} \leq k \leq 10^{-10}$ is representative of the soil permeability
 518 at Manitou Experimental Forest (see Appendix B) and the assignment of a value of 100
 519 Pa to Δp_β provides a reasonable estimate of the combined amplitudes of diurnal and semi-
 520 diurnal tides (e.g., Mass et al. (1991); Y. Li and Smith (2010); Marty et al. (2010)).

521 Nonetheless, this estimate of $|v_{pL}|$ is clearly sensitive to Δp_β (or to be more pre-
 522 cise $\partial p_\beta / \partial t$) and Δp_β can take on a variety of values associated with variety of differ-
 523 ent low frequency atmospheric phenomena. For example, J. Massmann and Ferrier (1992)
 524 use a pressure amplitude of about 2400 Pa (24 mb) and a period of 24 hours for their
 525 simulations. Although such large drops in surface pressure are certainly possible, they
 526 are extremely rare on a synoptic scale (i.e., during a 24 hour period). Drops in surface
 527 pressure at rates ≥ 1 mb hr⁻¹ or ≥ 100 Pa hr⁻¹ on the synoptic scale are usually as-
 528 sociated with bombogenesis (e.g., Sanders and Gyakum (1980)), i.e, the genesis of Bomb
 529 Cyclones and other types of severe weather. Otherwise, they do not characterize nor-
 530 mal ambient atmospheric conditions.

531 Clements and Wilkening (1974) use surface pressure observations that are more typ-
 532 ical of synoptic scale frontal passages in their study of advective velocities in soils. They
 533 found that $\partial p_\beta / \partial t = -65$ Pa hr⁻¹ and 50 Pa hr⁻¹, which on a 24-hour basis would cor-
 534 respond to $|\Delta p_\beta| \approx 1200 - 1600$ Pa. Further, using $k = 10^{-12}$ m² and $P \approx 86$ kPa,
 535 Clements and Wilkening (1974) estimate $|v_{pL}| \approx 100 \times 10^{-6}$ ms⁻¹. Given these data
 536 it should come as no surprise that Clements and Wilkening (1974) estimate $|v_{pL}|$ exceeds,
 537 by at least an order of magnitude, $|v_{pL}|$ given above. But, more importantly though is
 538 that Clements and Wilkening’s (1974) estimate of $|v_L|$, which is associated with frontal
 539 passages, supports the reasonableness of our estimate of $|v_L|$ associated with diel baro-
 540 metric forcing.

541 The assumption of a depth-attenuated sinusoidal solution underlying the estimates
 542 of v_T and v_{pL} works well because it is a valid linear solution to the linear parabolic equa-
 543 tions that describe $T_K(t, z)$ and $p_\beta(t, z)$. Such an approach will not necessarily work as
 544 well with the Muskat and Approximate models because they are nonlinear hyperbolic
 545 equations, for which numerical methods are preferred. Nonetheless, there is some value
 546 in adapting this linear approach to these two nonlinear models because it does offer in-
 547 sights into these two nonlinear models, their relationship to one another and how v_p es-
 548 timated with these two models compare to $|v_T|$, $|v_\theta|$ and $|v_{pL}|$.

549 Estimating v_p for the Muskat model (i.e., v_{pM}) follows immediately from express-
 550 ing the Muskat model in terms of velocity, i.e., $\partial p_\beta / \partial t - (P/\kappa)v_{pM}^2 = 0$. Substituting
 551 $\omega \Delta p_\beta$ for $\partial p_\beta / \partial t$ and solving for v_{pM} and then the order of magnitude estimate yields

$$|v_{pM}| = \sqrt{\omega \kappa \Delta p_\beta / P} = (30 - 300) \times 10^{-6} \text{ ms}^{-1}$$

552 This range of values for $|v_{pM}|$ is well supported by their agreement with the estimate
 553 of $|v| \sim (28 - 990) \times 10^{-6}$ ms⁻¹ derived by Iakovleva and Ryzhakova (2003, Table 2)
 554 from soil Radon transport measurements.

555 The relationship between $|v_{pL}|$ and $|v_{pM}|$ can be made more explicit by taking the
 556 ratio of $|v_{pL}|$ to $|v_{pM}|$, which yields

$$\frac{|v_{pL}|}{|v_{pM}|} = \sqrt{2 \frac{\Delta p_\beta}{P}} \approx 0.045 \ll 1$$

557 where the numerical values results from assuming (as above) $\Delta p_\beta \sim 100$ Pa and $P =$
 558 10^5 Pa. This result clearly indicates to expect that $|v_{pL}| < \text{or} \ll |v_{pM}|$. But more in-
 559 terestingly, this relationship is not explicitly a function of frequency of the (oscillatory)
 560 forcing pressure. Therefore, this linear analysis yields a specific prediction regarding the
 561 velocities produced by the Linear and Muskat models, which is that the ratio of the mod-
 562 eled velocities increases with increasing Δp_β . Therefore, because the amplitude of at-
 563 mospheric pressure perturbations tends to decrease with increasing frequency it follows
 564 to expect that $|v_{pL}|/|v_{pM}|$ will be maximal at low frequencies and minimal at high fre-
 565 quencies. This theoretical result will be tested in a later section summarizing the var-
 566 ious models' responses to low, mid and high frequency forcing.

567 For the Approximate model to be valid $\kappa p_\beta / P \partial^2 p_\beta / \partial z^2 \ll (P/\kappa) v_{pM}^2$ must be
 568 true or equivalently that $(\kappa \Delta p_\beta / P) (\Delta p_\beta / D_p^2) \ll \omega \Delta p_\beta$. Assuming that D_p from the
 569 Linear model is also valid for the Approximate and Muskat (or non-linear) models and
 570 substituting the expression for D_p above into D_p^2 results in $(p_\beta / (2P)) \omega \Delta p_\beta \ll \omega \Delta p_\beta$,
 571 which is obviously true because $p_\beta / (2P) < p_\beta / P \approx 10^{-3} \ll 1$. The order of magni-
 572 tude estimate of v_{pA} follows by replacing the differential form of the Approximate model
 573 with the algebraic form as has been throughout this section. The result is

$$|v_{pA}| = |v_{pM}| \sqrt{1 + 2\Delta p_\beta / P} \approx |v_{pM}| \approx (30 - 300) \times 10^{-6} \text{ ms}^{-1}$$

574 The key takeaways at this point in the analysis are (1) the approximations neces-
 575 sary to justify the Linear and Approximate models are valid, (2) for low frequency sur-
 576 face forcing (i.e., with periods within a factor of five or so of the daily cycle) the follow-
 577 ing ordering of the models' advective velocities is:

$$578 \quad |v_\theta| < |v_T + v_\theta| \leq |v_T| \sim |v_{pL}| \ll |v_{pM}| \approx |v_{pA}| \quad (16)$$

579 and (3) because $|v_T| \sim |v_{pL}|$ it may not be possible to assume a priori that advective
 580 flows associated with temperature dynamics are small relative to those of pressure, es-
 581 pecially for low porosity soils, e.g., $k \leq 10^{-14} \text{ m}^2$. This supports the need to examine
 582 the interactions of temperature and pressure on the advective transport velocity with
 583 models based on Equations (13), (14) and (15). To that end, the linear analysis is ap-
 584 plied to Equation (13).

585 This requires replacing the differential equation, $\partial p_\beta / \partial t - \Lambda_t + P \partial v_p / \partial z - \Lambda_z v_p =$
 586 0 with the following algebraic one $\omega \Delta p_\beta - P \omega \Delta T_\beta / T_K = P v_{pL*} / D_p - P \Delta T_\beta / (T_K D_T) v_{pL*}$
 587 and solving for v_{pL*} ; where the subscript '*' refers to the pressure-induced velocity, v_{pL} ,
 588 that includes the temperature and moisture terms. But here we consider only the tem-
 589 perature effects on v_{pL} for the sake of simplicity. A bit of mathematical manipulation
 590 yields the following:

$$\omega D_p \frac{\Delta p_\beta}{P} \left(1 - \frac{P}{\Delta p_\beta} \frac{\Delta T_\beta}{T_K} \right) = \left(1 - \frac{D_p}{D_T} \frac{\Delta T_\beta}{T_K} \right) v_{pL*}$$

591 After assuming that $T_K \approx 300$ K and given all other previous estimates above for the
 592 other terms in this equation, it is straightforward to show that $(P/\Delta p_\beta)/(\Delta T_\beta/T_K) \gg$
 593 1 and $(D_p/D_T)/(\Delta T_\beta/T_K) \gg 1$, from which it follows immediately that

$$|v_{pL*}| = \frac{D_T}{D_p} \frac{P}{\Delta p_\beta} |v_{pL}| = \sqrt{\frac{\kappa_T}{\kappa}} \frac{P}{\Delta p_\beta} |v_{pL}| = C_{L*} |v_{pL}| \sim (0.4 - 9) \times |v_{pL}|$$

594 where $\kappa_T = (0.1 - 0.7) \times 10^{-6} \text{ m}^2\text{s}^{-1}$ is the soil's thermal diffusivity (e.g., Campbell
 595 and Norman (1998, p. 124)). For the present purposes the principal determinant of the
 596 coefficient C_{L*} is $1/D_p$ or κ , the soil's pressure diffusivity. Meaning that as permeabil-
 597 ity decreases the temperature (and moisture) effects become increasingly more impor-
 598 tant, confirming the conclusion of the linear analysis of the individual velocities, $|v_T|$,
 599 $|v_\theta|$, and $|v_p|$ above. This last relationship also suggests that in terms of absolute mag-
 600 nitudes, it seems reasonable to conclude that either $|v_{pL*}| \sim |v_{pL}|$ or $|v_{pL*}| \geq |v_{pL}|$
 601 is more likely than $|v_{pL*}| < |v_{pL}|$. Nevertheless, by this linear analysis $|v_{pL*}| < |v_{pL}|$
 602 cannot be ruled out.

603 Applying the linear analysis to estimate $|v_{pM*}|$ from Equation (14) and $|v_{pA*}|$ from
 604 Equation (15)) yields estimates of C_{M*} and C_{A*} ranging (conservatively) between 10^{-2}
 605 to 10^2 . Interpreting such a wide range of possibilities is difficult. Nevertheless, this does
 606 suggest that the nonlinear models may be more sensitive to the temperature and mois-
 607 ture dynamics than the linear model. Further comparisons between all of these induced
 608 advective velocities is deferred until the discussion of the numerical results.

609 **2.2.3 A semi-observationally-based approach to estimating v_p**

610 This section outlines semi-observationally-based approach, based on vertically in-
 611 tegrating the conservation of mass (the COM approach), for estimating the advective
 612 velocities. It provides an alternative method that complements the three models outlined
 613 above. It follows from an approach similar to that employed by Parlange et al. (1998)
 614 and Novak (2016) for assessing how the diel cycle of v_T and v_θ might influence rates of
 615 soil moisture evaporation.

616 By integrating the 1-D version of Equation (2) over depth (after disregarding \mathbf{J} and
 617 S_a as discussed) the COM approach becomes

$$618 \quad Q_a(z=0) - Q_a(z_r) = - \int_{z_r}^{z=0} \left(\frac{\partial((\eta - \theta)Q_a)}{\partial t} \right) dz \quad (17)$$

619 where $Q_a = (\eta - \theta)Q_a v$ ($\text{mol m}^{-2}\text{s}^{-1}$) is the advective soil air mass flux, z_r (m) is a
 620 reference depth in the soil and $z = 0$ refers to the soil surface. Because this study uses
 621 $v(0)$ as a metric for assessing the relative performance of the three different models z_r
 622 is chosen to be the lower boundary of the model domain = 20 m at which the soil per-
 623 meability (discussed in the next section) becomes small enough to assume that $|Q_a(z =$
 624 $0)| \gg |Q_a(z_r)|$ or $|v(z = 0)| \gg |v(z_r)|$. With this lower boundary condition and the
 625 ideal gas law, Equation (17) can be solved for $v(0)$ to yield

$$626 \quad v(0) = - \frac{1}{(\eta(0) - \theta(0))Q_a(0)} \int_{z_r}^{z=0} \left((\eta - \theta) \frac{Q_a}{P_a} \frac{\partial p_\beta}{\partial t} - (\eta - \theta) \frac{Q_a}{T_K} \frac{\partial T_\beta}{\partial t} - Q_a \frac{\partial \theta_\beta}{\partial t} \right) dz \quad (18)$$

627 Equation (18) has the advantage of being linear in the forcing functions related to
 628 pressure, temperature and moisture. Therefore, it is also possible to identify $v_p(t, 0)$, $v_T(t, 0)$
 629 and $v_\theta(t, 0)$ as follows:

$$630 \quad v_p(0) = - \frac{1}{(\eta(0) - \theta(0))Q_a(0)} \int_{z_r}^{z=0} \left((\eta - \theta) \frac{Q_a}{P_a} \frac{\partial p_\beta}{\partial t} \right) dz \quad (19)$$

$$v_T(0) = \frac{1}{(\eta(0) - \theta(0))\varrho_a(0)} \int_{z_r}^{z=0} \left((\eta - \theta) \frac{\varrho_a}{T_K} \frac{\partial T_\beta}{\partial t} \right) dz \quad (20)$$

and

$$v_\theta(0) = \frac{1}{(\eta(0) - \theta(0))\varrho_a(0)} \int_{z_r}^{z=0} \left(\varrho_a \frac{\partial \theta_\beta}{\partial t} \right) dz \quad (21)$$

where the analytical models for $T_K = T_K(t, z)$, $T_\beta = T_\beta(t, z)$, $\theta = \theta(t, z)$ and $\theta_\beta = \theta_\beta(t, z)$ (detailed above) are used with Equations (18) - (21). Note for consistency with previous notation that $v_{T\theta}(0) = v_T(0) + v_\theta(0)$ and $v_{p*}(0) = v_p(0) + v_T(0) + v_\theta(0)$.

To estimate $v_p(0)$ requires an model of $p_\beta(t, z)$, which here is the product of the upper boundary condition on pressure $p_\beta(t, 0)$ and an analytical expression for the attenuation of the surface pressure signal with depth. Thus $p_\beta(t, z) = p_\beta(t, 0) \exp(-z/D_p)$, where now D_p depends on frequency range of the input signal. For low frequencies, $D_p \equiv D_{p,low} = 75$ m, for the mid range $D_p \equiv D_{p,mid} = 30$ m and for the high frequencies $D_p \equiv D_{p,high} = 1$ m. Although reasonable (as will be discussed further in section 4), these estimates of D_p are at this point “best guess only”. Of the three only $D_{p,mid}$ could be estimated from the profile of observed soil pressures, i.e., the surface pressure plus pressure measurements at 0.1 m, 0.2 m and 0.5 m. Given the relatively shallow depths of the measurements compared to the magnitude of $D_{p,mid}$ and the fact that the sensor at 0.5 m was intermittent $D_{p,mid} = 30$ m is certainly plausible, but highly uncertain. Even less certain are the estimates of $D_{p,low}$ and $D_{p,high}$. $D_{p,low}$ is scaled from $D_{p,mid} = 30$ m by a frequency ratio of the low and mid frequencies and $D_{p,high} = 1$ m is obtained from near-surface soil permeability measurements at MEF (Appendix B) and by assuming that the dominant high frequency pressure forcing has a period of 1-3 minutes. Given the large uncertainties inherent in these estimates of D_p , each is compared with the numerical results. Finally, $\partial p_\beta(t, z)/\partial t$ is computed numerically using a third order finite difference scheme, $\partial p_\beta(t, z)/\partial z$ is computed analytically and the integration uses MatLab subroutines.

3 Site Description, Instrumentation, and Data

Manitou Experimental Forest (39° 04' N and 105° 04' W) is a dry montane ponderosa pine (*Pinus ponderosa*) forest in the central Rocky Mountains about 45 km west of Colorado Springs, CO, USA. MEF has a mean elevation of about 2400 m ASL, an annual mean temperature of about 5 C and an annual precipitation of about 400 mm. Previous grazing and mechanical harvesting throughout the area has resulted in a moderately disturbed soil. Soil organic matter comprises about 1-2% of the soil by mass and is more or less uniform through at least the top 10 cm of soil. The dominant parent materials of the soils within MEF are primarily Pikes Peak granite and secondarily weathered red arkostic sandstone. Typical soil within MEF is a deep (> 1.0 m), fine-loamy, mixed, frigid, Pachic Argiustoll and tend to have low available water holding capacity and a (moderately high) permeability – ranging between about 1×10^{-12} and 250×10^{-12} within the top 1 m of the soil. Typical MEF soils range between 60-65% sand, 20-25% silt, and 10-15% clay with bulk densities that usually increase with depth and range between 1.1 Mgm^{-3} and about 1.6 Mgm^{-3} . For modeling purposes the vertical structure for the soil permeability, $k_u(z)$, and bulk density, $\rho_s(z)$, are derived from measurements of their vertical profiles obtained in the upper 1 m of soil at MEF (see Appendix B). These analytical functions are $k_u(z) = 10^{-12}(126 \tanh(6(z - 0.95)) + 132.4) \text{ m}^2$ in the upper 1.5 m and as $k(z) = k_u(z = 1.5) \exp(-(z - 1.5))$ for $1.5 \text{ m} \leq z \leq 20 \text{ m}$ and $\rho_s(z)$, as $1.65 + \sin(\pi(z + 7/60))(\tanh(4(z - 0.72)) - 1)/3 \text{ Mgm}^{-3}$ throughout the domain. The model for the total soil porosity, $\eta = \eta(z)$, follows directly from the $\rho_s(z)$, i.e., $\eta(z) =$

677 $1 - \rho_s(z)/\rho_p$, where $\rho_p = 2.65 \text{ Mgm}^{-3}$ is the particle density for the sandy MEF soils,
 678 which is assumed to be constant throughout the domain.

679 The data supporting the present study is part of a larger (multi-purposed) field cam-
 680 paign performed between December 2008 and August 2014 (Frank & Massman, 2020).
 681 The specific site was on a gentle east facing slope about 1.2 km west of the Manitou Ex-
 682 perimental Forest headquarters in an opening covered primarily by bunchgrasses, but
 683 with a few scattered trees throughout. All sensors were confined to a 15 m \times 15 m plot.
 684 At the center of the plot was an elevated structure with control boxes, dataloggers, so-
 685 lar panels, and batteries. Replicate soil pits were located in four directions about 4 m
 686 from the center. Each replicate had three pits, the first was about 1.3 m deep for tem-
 687 perature (and thermal conductivity probes, which are not discussed in the present study),
 688 a second for soil moisture probes that was about 1 m deep, and a third one for soil CO₂
 689 probes that was about 1 m deep (which are not discussed here either). A final pit was
 690 dug for soil pressure sensors about 9 m east of the plot center that was about 1 m deep
 691 and large enough to hold a 0.5 m \times 0.5 m sensor/control box. Profiles of the within-pore
 692 air pressure were sampled and recorded at 1 Hz at 0, 10, 20, and 50 cm with a differ-
 693 ential pressure sensor (Appendix C). Profiles of soil temperature and soil moisture were
 694 measured and recorded every 5 minutes. Temperatures were measured with thermocou-
 695 ples at the soil surface and at 0.5, 1.5, 2.5, 3.5, 7.5, 12.5, 17.5, 25.0, 75.0, and 125.0 cm
 696 depths at four locations. Soil moisture was measured with TDRs (Time Domain Reflec-
 697 tometers) at 2.0, 5.0, 10.0, 15.0, 20.0, 50.0, 100.0 cm also at the same four locations. The
 698 full profiles of temperature and the soil moisture are important to the present study be-
 699 cause they were used to check that the models for $T_\beta(t, z)$, $\theta_\beta(t, z)$, $\Lambda_t(t, z)$ and $\Lambda_z(t, z)$
 700 (discussed in section 2.1.2 above) were reasonably consistent with the observed profiles.

701 Further details of the instrumentation and the experiment can be found in (Frank
 702 & Massman, 2020) and Appendix C, which summarizes the details about the pressure
 703 sensors and how the 1 Hz differential pressure data were calibrated against and merged
 704 with the low frequency (ambient) data used in the following section.

705 4 Results and Discussion

706 This study focuses on two periods in 2012: June 14-20 (144 hours) and October
 707 2-13 (250 hours). The observationally-based surface forcing functions, $p_\beta(t, 0)$, $T_\beta(t, 0)$
 708 and $\theta_\beta(t, 0)$ are shown in Figures 1 (June) and 2 (October). The conservation of mass
 709 approach, Equations (18)-(21), and each of the three numerical models, Equations (7),
 710 (10), and (11), were used to estimate the surface velocity, $v(t, 0)$ and the standard de-
 711 viation of the surface velocity, $\sigma_v(0)$, for each period with pressure-only forcing and with
 712 pressure plus temperature and moisture effects. (Note: Henceforth $|v|$ or $|v(0)|$ (from the
 713 Linear Analysis section and understood here as the amplitude of a time series) and the
 714 standard deviation, σ_v or $\sigma_v(0)$, are used synonymously because for sinusoidal time se-
 715 ries the amplitude and standard deviation are linearly related by $\sqrt{2}$.) All resulting stan-
 716 dard deviations can be found in Table 1 including those associated with using the un-
 717 filtered 1 Hz surface data (all frequencies) and the filtered (low, mid, and high frequen-
 718 cies) surface pressure data as the upper (surface) boundary condition. Table 1 also in-
 719 cludes $\sigma_{v_T}(0)$, $\sigma_{v_\theta}(0)$ and $\sigma_{v_{T\theta}}(0)$ and the results of a sensitivity analysis of $\sigma_{v_p}(0)$ to
 720 changes to the numerical value of $D_{p,high}$. The numerical results concerning $v(t, 0)$ are
 721 shown and discussed in the next two sections.

722 4.1 Low frequency forcing: Periods ≥ 5 hours

723 Figure 3 shows the COM estimates of $v_p(0)$ from Equation (19), $v_T(0)$ from Equa-
 724 tion (20) and $v_\theta(0)$ from Equation (21) for the June 2012 study period. The takeaways
 725 here are that (1) $|v_p| \gg |v_T|$ and $|v_\theta|$, as might be expected for a soil with a perme-
 726 ability $> 10^{-12} \text{ m}^2$, and (2) the COM estimate of $|v_T|$ agrees more closely with Kim-

727 ball (1983) than with the estimated based of the thermally induced flow (Section 2.2.1
 728 above). A less obvious takeaway is that during periods of rain (also see Figure 1 and in
 729 particular Figure 2) that $|v_\theta| \approx |v_T|$. In fact the corresponding figure for the October
 730 study period (not shown) would even indicate that $|v_\theta| > |v_T|$, a conclusion supported
 731 by the results shown in Table 1 (Low Frequencies column). There are two contributing
 732 factors to the unexpected reversal of this inequality. (a) v_T is smaller in magnitude dur-
 733 ing the October period than the June period because the soil is heated less strongly by
 734 the daily heating cycle during October than June (compare amplitudes of the soil sur-
 735 face temperatures shown in Figures 1b and 2b). (b) Although it is possible that lack of
 736 a temperature correction to the TDR may be contributing biased estimates of $\partial\theta/\partial t$ and
 737 $\partial\theta/\partial z$, there are two more important reasons why $|v_\theta|$ is relatively large during the Oc-
 738 tober study period. First, rainfall amounts and rates were higher than during the June
 739 period and (2) the air filled pore space – the denominator of Equation (21), $\eta(0)-\theta(0)$
 740 – is smaller during the October period, which will tend to increase $|v_\theta|$.

741 These low frequency results from the COM approach are echoed in $\sigma_v(0)$ in Table
 742 1. In addition, this table further suggest that $\sigma_{v_{T\theta}} < \sigma_{v_T} + \sigma_{v_\theta}$, thereby supporting
 743 the notion that there is some phase difference between v_T and v_θ and that during a typ-
 744 ical diel cycle the temperature and moisture effects tend to act (at least weakly) in op-
 745 position to one another. But Table 1 also indicates that v_θ can be surprisingly large (rel-
 746 ative to v_T), undoubtedly due (at least in part) to rapid changes in soil moisture asso-
 747 ciated with rain. Finally, the influence of soil heating and moisture dynamics on $|v_p|$ (see
 748 Equation (18)) is also presented in Table 1 (by comparing σ_{v_p} with $\sigma_{v_{p*}}$ in the All and
 749 Low Frequencies columns). Overall temperature and moisture effects do not have much
 750 impact on the pressure pumping velocity for the COM approach. But during periods of
 751 rapid changes in θ soil moisture dynamics may be important enough to consider, espe-
 752 cially if the soil is moist to begin with or if the soil permeability is $< 10^{-12}$ m².

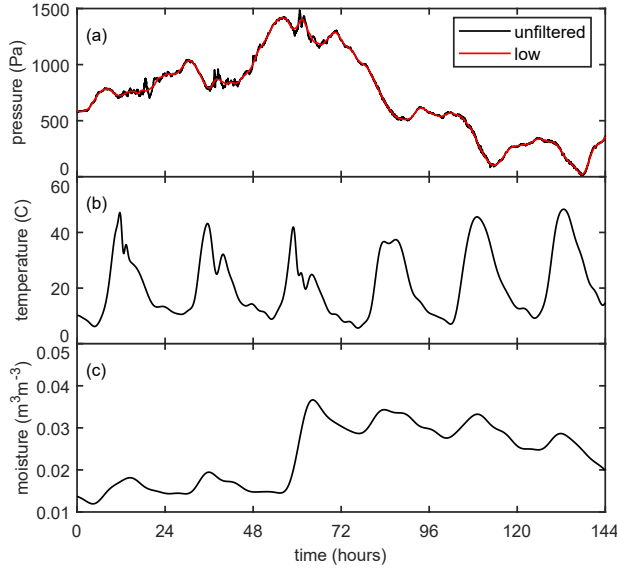


Figure 1. Model drivers (or surface forcing functions) for the June 14-20, 2012 simulation. (a) The black line is the observed 1 Hz surface pressure data, $p_{\beta}(t, 0)$, which has had enough of the background pressure removed to ensure all data are ≥ 0 . The red line is the numerically filtered low frequency component of the surface pressure and includes only those data with periods ≥ 5 hours. (b) 1 Hz temperature forcing function, $T_{\beta}(t, 0)$, interpolated from the observed 5 minute averages of the soil surface temperatures. The frequency content of this forcing is limited almost exclusively to low frequencies with only a small component of mid frequency content (i.e., periods between 0.5 and 5 hours). (c) 1 Hz soil moisture forcing function, $\theta_{\beta}(t, 0)$, interpolated from the observed 5 minute averages of the 2-cm volumetric soil moisture. This forcing is exclusively low frequency because the mid and high frequency content (i.e., with periods between 1 s and 0.5 hours) was low amplitude noise that has no influence on the numerical results.

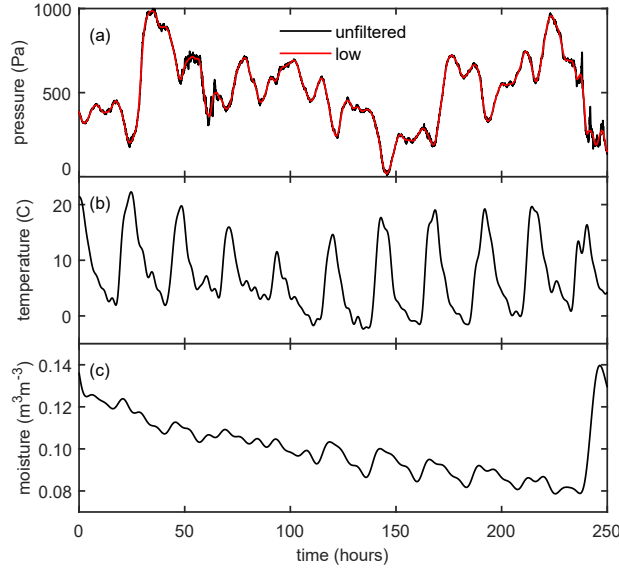


Figure 2. Model drivers (or surface forcing functions) for the October 2-13, 2012 simulation. (a) The black line is the observed 1 Hz surface pressure data, $p_{\beta}(t, 0)$, which has had enough of the background pressure removed to ensure all data ≥ 0 . The red line is the numerically filtered low frequency component of the surface pressure and includes only those data with periods ≥ 5 hours. (b) 1 Hz temperature forcing function, $T_{\beta}(t, 0)$, interpolated from the observed 5 minute averages of the soil surface temperatures. The frequency content of this forcing is limited almost exclusively to low frequencies with only a small component of mid frequency content (i.e., periods between 0.5 and 5 hours). (c) 1 Hz soil moisture forcing function, $\theta_{\beta}(t, 0)$, interpolated from the observed 5 minute averages of the 2-cm volumetric soil moisture. This forcing is exclusively low frequencies because the mid and high frequency content (i.e., with periods between 1 s and 0.5 hours) was low amplitude noise that has no influence on the numerical results.

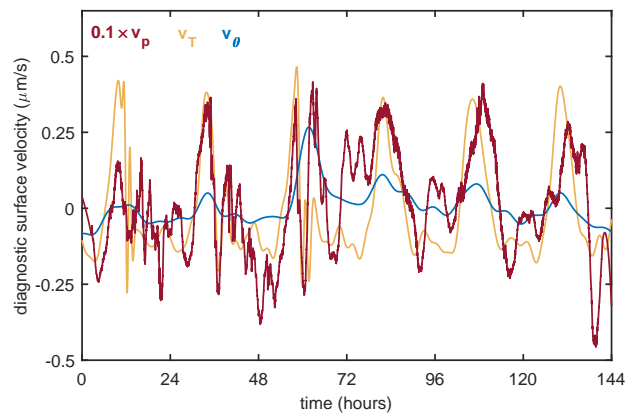


Figure 3. Estimates of low frequency advective velocities induced by pressure, temperature and soil moisture dynamics using the COM approach (Equations (19), (20), and (21)) for June 14-20, 2012. As discussed in the text, the soil temperature and moisture forcing functions, and therefore, v_T and v_θ as well, are for all numerical purposes low frequency only.

Table 1. Standard deviation of soil surface advective velocity variance: $\sigma_v(0)$ (μms^{-1}). The subscript * denotes the inclusion of the temperature and moisture effects. ^a $\sigma_{v_{T\theta}} = \sigma(v_T + v_\theta)$; ^b $\sigma_{v_p} = \sigma(v_{p,low} + v_{p,mid} + v_{p,high})$; ^c $\sigma_{v_{p*}} = \sigma(v_{p,low} + v_{p,mid} + v_{p,high} + v_T + v_\theta)$. Note that numerical estimates for $\sigma_{v_T}(0)$, $\sigma_{v_\theta}(0)$ and $\sigma_{v_{T\theta}}(0)$ are the same for All Frequencies and Low Frequencies. This is because the frequency content of soil temperature and moisture is overwhelmingly low frequencies. The column relating to $D_{p,high}$ is part of a sensitivity analysis regarding the COM's estimates of v_p .

Model	All Frequencies		Low Frequencies		Mid+High Frequencies		Mid Frequencies		High Frequencies		$D_{p,high}$ (m)
	06/2012	10/2012	06/2012	10/2012	06/2012	10/2012	06/2012	10/2012	06/2012	10/2012	
<i>COM</i>											
σ_{v_T}	0.17	0.07	0.17	0.07	—	—	—	—	—	—	—
σ_{v_θ}	0.06	0.11	0.06	0.11	—	—	—	—	—	—	—
$\sigma_{v_{T\theta}}$	0.20 ^a	0.14 ^a	0.20 ^a	0.14 ^a	—	—	—	—	—	—	—
σ_{v_p}	5.6 ^b	5.5 ^b	1.7	2.7	—	—	2.3	2.7	4.8	4.0	1.0
$\sigma_{v_{p*}}$	5.7 ^c	5.6 ^c	1.9	2.7	—	—	—	—	—	—	—
σ_{v_p}	—	—	—	—	—	—	—	—	2.7	2.1	0.5
σ_{v_p}	—	—	—	—	—	—	—	—	3.6	4.4	0.9
σ_{v_p}	—	—	—	—	—	—	—	—	9.1	7.7	2.0
<i>Linear</i>											
$\sigma_{v_{pL}}$	4.4	4.1	1.5	1.8	4.2	3.6	1.8	1.7	3.7	3.2	—
$\sigma_{v_{pL*}}$	3.0	2.6	0.9	1.0	—	—	—	—	—	—	—
<i>Muskat</i>											
$\sigma_{v_{pM}}$	21	18	19	15	10	8.8	5.2	5.2	8.5	7.1	—
$\sigma_{v_{pM*}}$	12	210	11	210	—	—	—	—	—	—	—
<i>Approximate</i>											
$\sigma_{v_{pA}}$	19	15	17	13	9.7	8.4	4.7	4.6	8.5	7.0	—
$\sigma_{v_{pA*}}$	11	175	10	175	—	—	—	—	—	—	—

Figure 4 compares (for June 2012) $v_p(t, 0)$ from the COM approach (i.e, the COM approach and Equation (19)) with solutions from the Linear model, $v_{pL}(t, 0)$ from Equation (7), the Muskat model, $v_{pM}(t, 0)$ from Equation (10), and the Approximate model, $v_{pM}(t, 0)$ from Equation (11). Figure 5 is the analog to Figure 4, except for the inclusion of the soil temperature and moisture dynamics in the solution, i.e., $v_{pL^*}(t, 0)$ from Equation (13), $v_{pM^*}(t, 0)$ from Equation (14) and $v_{pM^*}(t, 0)$ from Equation (15)). Comparing the first 80 hours of these two simulations indicates that the temperature and moisture effects can alter the phase of the velocity or even reverse it completely and Table 1, which summarizes all low frequency modeling results for both the June and October 2012 observation periods, indicates that they can also affect the amplitude. With respect to the modeling results the important observations to make are (1) including heat and moisture effects with the two nonlinear models yield very different solutions for the October 2012 case than the June 2012 case. Otherwise, (2) for the June 2012 case the advective velocity associated with both the linear and nonlinear models decreases with the inclusion of temperature and moisture effects (i.e., $\sigma_{v_{pL^*}} < \sigma_{v_{pL}}$, $\sigma_{v_{pM^*}} < \sigma_{v_{pM}}$, $\sigma_{v_{pA^*}} < \sigma_{v_{pA}}$), whereas the COM approach (very weakly) suggests just the opposite, (3) the Linear model and the COM approach produce velocities of a similar magnitude and phase but both are smaller in magnitude by a factor of 2 to 5 than either the Muskat or Approximate models and (4) the advective velocities associated with the Muskat model exceed those of the Approximate model. Some of these observations are valid for the October 2012 case as well, but the real difference is that for the October case $\sigma_{v_{pM^*}}$ and $\sigma_{v_{pA^*}}$ not only exceed $\sigma_{v_{pM}}$ and $\sigma_{v_{pA}}$, but they both exceed $100 \mu\text{ms}^{-1}$, (possibly) contrary to expectations.

Accepting these unexpected results at face value suggests that temperature and moisture dynamics cannot always be ignored in the nonlinear models. But, to better understand this anomalous result a sensitivity analysis was performed that indicated that the nonlinear models' (Equations (14) and (15)) solutions were quite sensitive to the magnitude and vertical structure of Λ_z , but much less sensitive to variations in Λ_t . Regardless though none of these tests fully eliminated this seeming contradiction. However further insight into this quandary can be found in section 4.3, which deals with the models' profiles of pressure and advective velocity. Presumably additional insights might also be possible with a model that fully couples soil heating and moisture dynamics (rather than prescribing them as done here), but this avenue is beyond the purposes of the present study.

In addition to Table 1, the present (all and low frequency) results can be summarized by replacing Equation (16) with the following, more precise ordering of model advective velocities:

$$|v_\theta| \approx |v_T| \leq |v_{T\theta}| \ll |v_{pL^*}| \leq |v_{pL}| \leq |v_p| \approx |v_{p^*}| < \text{or} \ll |v_{pA}| \approx \text{or} < |v_{pM}| \quad (22)$$

and

$$|v_{pA^*}| < |v_{pM^*}|$$

where \ll signifies at least one order of magnitude difference and the relationships between $|v_{pA}|$ and $|v_{pA^*}|$ and $|v_{pM}|$ and $|v_{pM^*}|$ remain difficult to generalize with any certainty. But maybe this should not be unexpected. Recall that the linear analysis of section 2.2.2 was also unable to offer any easily generalized insights into what might be expected from any of the three models regarding the impact of including the heat and moisture effects on the relative magnitudes of their advective velocities.

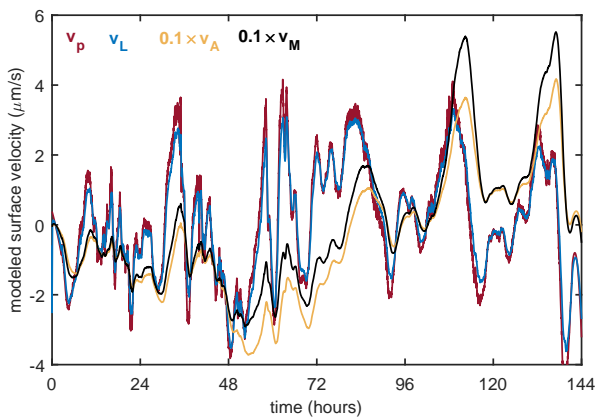


Figure 4. Estimates of low frequency advective velocities induced by pressure dynamics only using the Linear model (v_L , Equation (7)), the Muskat model (v_M , Equation (10)) and the Approximate model (v_A , Equation (11)) for June 14-20, 2012. v_p from the COM, Equation (19) is included for comparison.

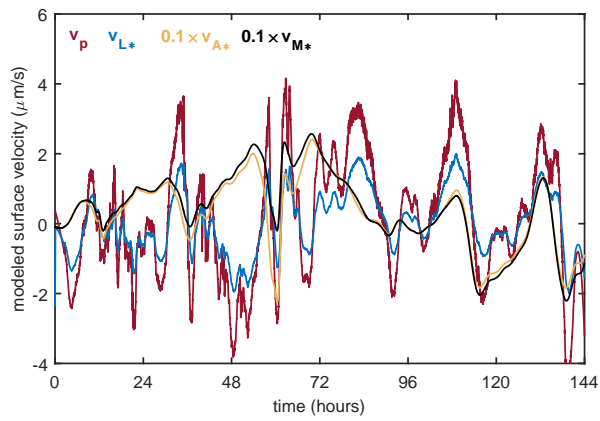


Figure 5. Estimates of low frequency advective velocities induced by pressure, temperature and soil moisture dynamics combined using the Linear model (v_{L*} , Equation (13)), the Muskat model (v_{M*} , Equation (14)) and the Approximate model (v_{L*} , Equation (15)) for June 14-20, 2012. v_p from the COM, Equation (19) is included for comparison.

798 But the implications of Table 1 extend beyond Equation (22). Recalling the dis-
 799 cussion of the threshold velocity of $100 \mu\text{ms}^{-1}$ (Section 2) and focusing on the COM ap-
 800 proach and the linear model, it is possible to conclude that soil temperature and mois-
 801 ture dynamics are unlikely to ever play a role in advective flow in soils. Considering that
 802 Parlange et al. (1998) used the COM approach to conclude that temperature dynam-
 803 ics are a potentially significant contributor to advective flows in soils, the present results
 804 concur with Novak (2016), who pointed out that Parlange et al. (1998) must have made
 805 a computational error. Nonetheless, without further insights into causes of the unexpected
 806 results from the nonlinear models for the October 2012 case, the possibility remains that
 807 soil heating and moisture dynamics (Λ_z in particular) may enhance the advective ve-
 808 locities associated with pressure pumping enough (at least for the nonlinear models) that
 809 they might contribute to soil evaporation and the surface energy balance (i.e., $v_{pM^*} >$
 810 $100 \mu\text{ms}^{-1}$ and $v_{pA^*} > 100 \mu\text{ms}^{-1}$).

811 4.2 Mid (0.5 - 5 hrs) and high (1 s - 0.5 hrs) frequency forcing

812 Figure 6a shows a wavelet decomposition of the June 14-20, 2012 surface pressure
 813 after removal of the low frequency component. Figures 6b and 6c are (in order) the band-
 814 pass filtered mid and high frequency pressure components. This 6 day period can be par-
 815 titioned into before (0–72 hours) and after (72–144 hours) a frontal passage (see the UCAR
 816 weather archives at <https://www2.mmm.ucar.edu/imagearchive/>) with rain falling for
 817 a short time beginning at about hour 60 (MEF headquarters building rain gauge). The
 818 three pressure events preceding the frontal passage are self-identified here as inertia-gravity
 819 waves (or possibly other related types of mesoscale gravity waves), whereas after the frontal
 820 passage the pressure perturbations are interpreted as a “typical” diel cycle of turbulence
 821 and other high frequency atmospheric phenomena. The presence of inertial gravity waves
 822 during this period of frontal activity and associated convective activity is almost a cer-
 823 tainty (e.g., Koch and Siedlarz (1999); Ralph et al. (1999); Koppel et al. (2000); Rup-
 824 pert and Bosart (2014); X. Wang et al. (2020)). Further fitting a Morlet function (mod-
 825 ulated wave packet) to each of these inertia gravity wave events yields wave periods be-
 826 tween about 2.1 and 2.5 hours with amplitudes between approximately 30 and 70 Pa,
 827 which are very similar to the low frequency gravity waves observed in China by X. Wang
 828 et al. (2020) and very similar to an inertia-gravity wave’s theoretical period of about 2.7
 829 hours (at 45° N latitude) suggested by Fritts and Alexander (2003).

830 Given the near ubiquity of inertia-gravity waves and their close association with
 831 convective frontal systems, Figure 7 examines how this phenomenon might influence ad-
 832 vective flows (at least in the MEF soils) by isolating the first 48 hours of the June 2012
 833 study period. This figure includes the mid frequency surface forcing and the modeled
 834 mid and high frequency response (surface velocities). The important takeaways from Fig-
 835 ures 6 and 7 are (1) the mid and high frequency velocities computed with the nonlin-
 836 ear models exceed by an order of magnitude the velocities produced by the linear model
 837 and the COM approach (also see Table 1), (2) both the mid and high frequency instan-
 838 taneous velocities are significant, often approaching or exceeding the critical $100 \mu\text{ms}^{-1}$
 839 velocity, especially with the nonlinear models for which the velocities can approach 1000
 840 μms^{-1} , (3) the mid frequency forcing events seem to intensify (or be associated with)
 841 some of the high frequency pressure forcing (including the diel cycle of turbulence), and
 842 (4) what might otherwise appear in a shorter time series as more-or-less random episodic
 843 pressure forcing events appear in these figures to result from causal atmospheric phenom-
 844 ena, which are often associated with frontal systems, thunderstorms and rain.

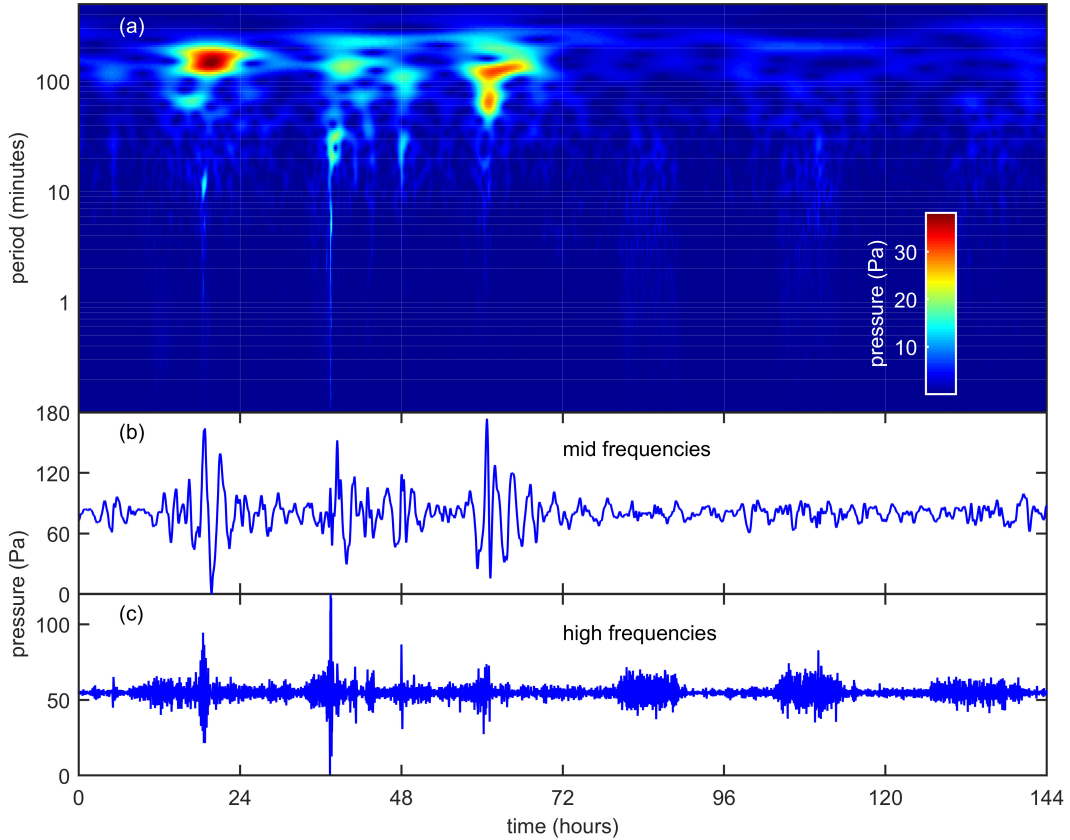


Figure 6. (a) Wavelet decomposition of the June 14-19, 2012, soil surface pressure time trace using the Morlet wavelet after removing the low frequencies, i.e., all frequencies with periods longer than 5 hours. (b) Filtered mid frequency (periods between 0.5 and 5 hours) surface pressure time series. (c) Filtered high frequency (periods between 1 s and 0.5 hours) surface pressure time series. Three (self-identified) inertia-gravity waves occur each day during the first 72 hours (June 14, 15, 16). Wave periods of these events (panels (b)) were between about 2.1 and 2.5 hours with maximum amplitudes between approximately 30 and 70 Pa. Rain fell about hour 60 (mid-day June 16). The daily pulses of high frequency surface pressure, panel (c), during the last 72 hours (June 17, 18, 19) are interpreted here as the diel cycle in turbulence, suggesting that the three wave events (panel (b)) intensify the diel cycle of turbulence. Finally, in addition to the inertia-gravity wave the second day (panel (b)) appears to include a slightly higher frequency gravity wave event centered at about 48 hours.

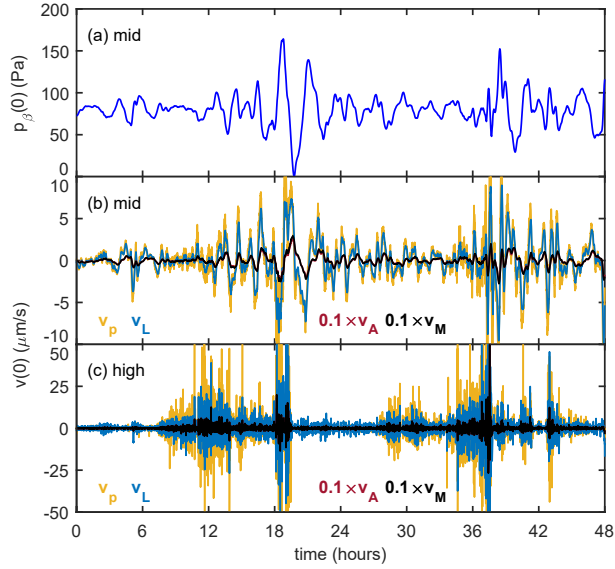


Figure 7. (a) First 48 hours of the June 2012 mid-frequency soil surface pressure time series. The surface pressure perturbations between approximately 16 and 24 hours and the more complex signal between about 36 and 48 hours are interpreted here as an inertia-gravity wave events. These two wave events coincide with the leftmost (first and second) ‘bright spots’ on Figure 6a. (b) First 48 hours of the modeled June 2012 mid frequency soil surface velocities and (c) first 48 hours of the modeled high frequency surface velocities. Because $v_A \leq v_M$, v_A is obscured by v_M in panel (c). All velocities highlight the impact that the inertia-gravity waves, shown in panel (a), can have on the soil advective velocity field. Note the episodic nature of the high frequency velocities, their (at least partial) association with the wave events, and that the high frequency velocities are often about an order of magnitude greater than the mid-frequency velocities.

845 Figures 8 and 9 are the October analog to the two preceding figures. Figure 8 sug-
 846 gests that an inertia gravity wave event occurred during each of the first two days of the
 847 October period (i.e., October 2 and 3). This wave activity occurred ahead of the pas-
 848 sage of a weak wind shift line and frontal system (UCAR weather archives:
 849 <https://www2.mmm.ucar.edu/imagearchive/>). The wave periods of these two events were
 850 between about 2.2 and 2.6 hours with amplitudes between approximately 20 and 60 Pa,
 851 quite similar to the June events. But Figure 8 also suggests something quite different
 852 appeared on the last day of the study period, October 13. The two obvious pressure spikes
 853 on that day (and possibly two or three less obvious spikes, which precede and follow the
 854 two major spikes) are here self-identified as atmospheric solitons. Solitons or solitary waves,
 855 are identified as either positive or negative pressure pulses (or spikes) and often associ-
 856 ated with fronts and thunderstorms (e.g., Shreffler and Binkowski (1981); Doviak and
 857 Ge (1984)). They can have amplitudes between about 10 and 200 Pa with a duration
 858 between about 10 minutes and 2 hours (e.g., Goncharov and Matveyev (1982); Hauf et
 859 al. (1996); Ruppert and Bosart (2014)). Figure 9 isolates these solitons (panel a) and
 860 the mid and high frequency modeled soil advective velocities in the last 25 hours of the
 861 October 2012 study period. The amplitudes of these two events are between about 80
 862 and 110 Pa with durations between about 1.6 and 2 hours. On this day there was sig-
 863 nificant frontal activity in the area (<https://www2.mmm.ucar.edu/imagearchive/>) with
 864 rain starting just in the early afternoon (MEF rain gauge). The takeaways from this Oc-
 865 tober period (i.e., last two figures) are the same as the June period, except that the in-
 866 tensification of the high frequency forcing and associated soil velocities by the mid fre-
 867 quency events is even stronger.

868 Figure 10 and Table 1 summarize the June and October modeling results for the
 869 three frequency ranges. Figure 10 especially highlights the difference between the non-
 870 linear and linear methods. First $\sigma_v(0)$ from the nonlinear models always exceed those
 871 predicted by linear methods and second, the ratio $\sigma_{vL}(0)/\sigma_{vM}(0)$ is much smaller at low
 872 frequencies than at mid or high frequencies. The first of these relationships was antic-
 873 ipated by the linear analysis discussed in section 2.2.2, but the second is opposite of what
 874 was predicted. Possibly this should not be too surprising because the linear analysis can-
 875 not fully describe the solutions of the nonlinear models. The interpretation of the results
 876 given in Figure 10 is that the nonlinear models produce significantly greater advective
 877 transport at low and high frequencies than at mid frequencies. In fact, the difference be-
 878 tween modeling results at low frequencies is so great that it is possible to conclude that
 879 pressure induced advective motions in soils is likely negligible for the linear model (con-
 880 trary to expectations), whereas just the opposite conclusion can be reached with the non-
 881 linear models. A complementary interpretation to this is that the linear methods pro-
 882 duce greater advective transport at the mid/high frequencies than at low frequencies.
 883 Overall, these rather different “spectral responses” again serve to emphasize that the lin-
 884 ear and nonlinear models are fundamentally different models of pressure pumping and,
 885 as a consequence, they yield different predictions for the advective velocities in perme-
 886 able media.

887 The point was made earlier that all the estimates for D_p used with the COM ap-
 888 proach were fairly uncertain. Consequently the estimates of the advective velocities as-
 889 sociated with the COM approach are also uncertain. This is especially true for high fre-
 890 quencies because the range of variation in D_p is greatest for high frequencies. To address
 891 this Table 1 includes estimates of the high frequency (COM) σ_{vp} for $D_p = 0.5$ m and
 892 $D_p = 2.0$ m. (Recall that $D_p = 1.0$ m is the original estimate (Table 1)). This sensi-
 893 tivity analysis (change in σ_{vp} with respect to change in D_p) for high frequencies qual-
 894 ifies the results shown in Figure 10. At least for high frequencies, even small change in
 895 a reasonable guess for D_p could yield an estimate of σ_{vp} that more closely resembles (or
 896 even exceeds) σ_{vPM} and σ_{vPA} (the nonlinear models) than σ_{vPL} (the Linear model). Con-
 897 sequently, imprecise knowledge of D_p only yields imprecise estimates of the advective
 898 velocity associated with the COM approach and any ability it may have to distinguish

899 between linear and nonlinear models is potentially lost, especially at high frequencies.
900 But the relationship between the COM, D_p , and $v_p(z)$ at high frequencies is more con-
901 fusing than might otherwise be expected from just this section.

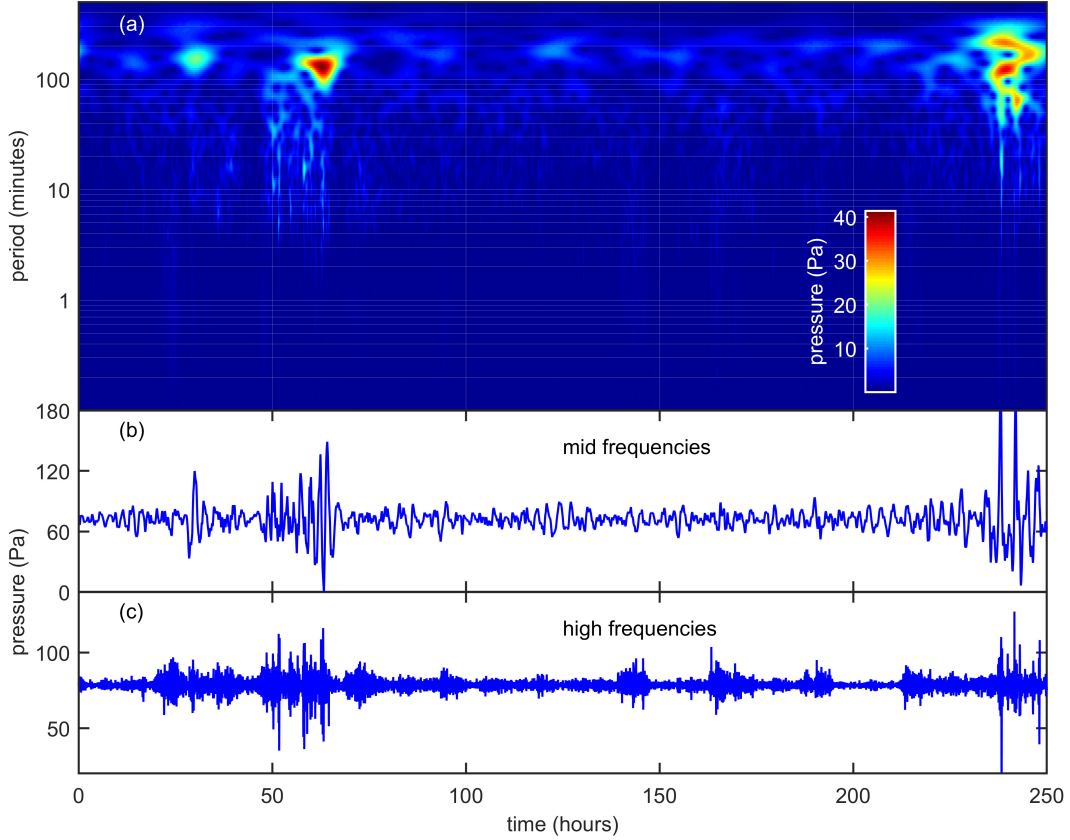


Figure 8. (a) Wavelet decomposition of the October 2-13, 2012, soil surface pressure time trace using the Morlet wavelet after removing the low frequencies, i.e., all frequencies with periods longer than 5 hours. (b) Filtered mid frequency (periods between 0.5 and 5 hours) surface pressure time series. (c) Filtered high frequency (periods between 1 s and 0.5 hours) surface pressure time series. Two (self-identified) inertia-gravity waves occur each day between (approximately) 24 and 72 hours (October 3 and 4). Wave periods of these two waves, panel (b), were between about 2.2 and 2.6 hours with maximum amplitudes between approximately 20 and 60 Pa. A pair of atmospheric solitons (also self-identified) appear as two positive spikes in panel (b), the mid-frequency time series, during the last 24 hours (October 13). The amplitudes of these two events are between about 80 and 110 Pa with durations between about 1.6 and 2 hours. Rain fell just after hour 240 (mid-day October 13). Similar to the June study period (Figure 6c), the diel cycle of turbulence is also present during the October period and again both the inertia-gravity waves and the solitons appear to intensify the high frequency turbulent surface pressure perturbations.

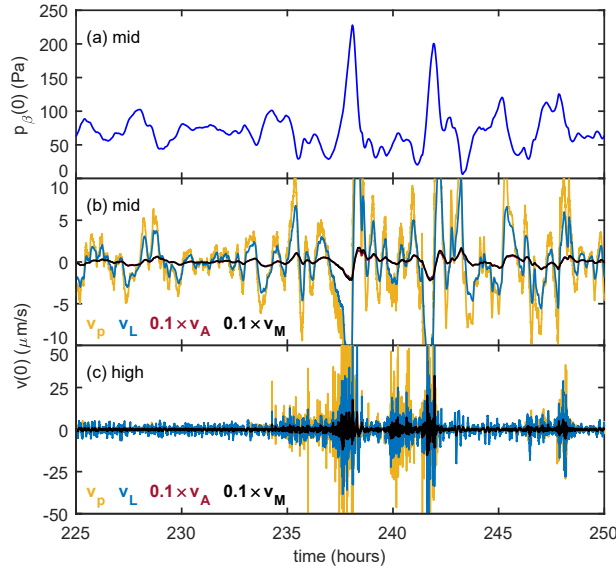


Figure 9. (a) Last 25 hours of the October 2012 soil surface pressure time series. The two pressure events centered at approximately 237 and 243 hours are interpreted here as solitons and they correspond to the rightmost (complex) ‘bright spot’ on Figure 8(a). (b) Last 25 hours of the modeled (b) mid frequency soil surface velocities and (c) high frequency soil surface velocity time series. Because $v_A \leq v_M$ v_A is obscured by v_M in panel (c). All velocities highlight the impact that the solitons, shown in panel (a), can have on the soil advective velocity field. Note the episodic nature of the high frequency velocities, their (relatively) strong association with the soliton events, and that the high frequency velocities are often about a factor of two or more greater in magnitude than the mid-frequency velocities.

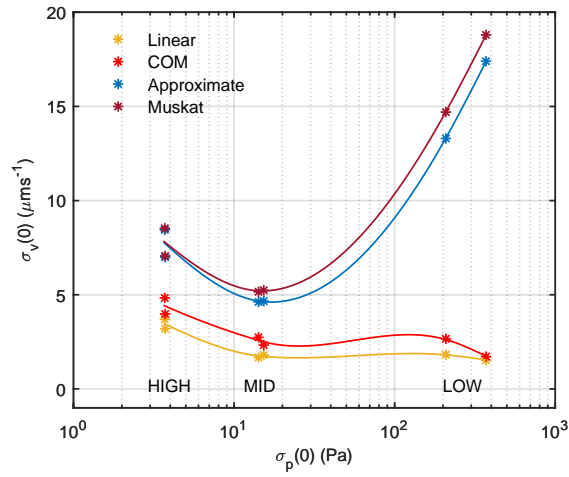


Figure 10. Summary plot of the response, $\sigma_v(0)$, vs the forcing, $\ln(\sigma_p(0))$, for the June and October study periods as a function of frequency band for the COM approach, the linear model and the two nonlinear models. Low frequencies refer to atmospheric pressure variations with periods ≥ 5 hours, mid frequencies have periods between 0.5 and 5 hours, and high frequencies have periods between 1 sec and 0.5 hours. Given that $\sigma_p(0)$ increases fairly strongly with decreasing frequency this plot can also be interpreted as a crude description of the different models' spectral response.

4.3 Vertical profiles of pressure and advective velocity

For the same surface forcing and permeability the reason the nonlinear models predict a higher amplitude for the advective velocities than the linear methods can be inferred from Figure 11, which shows the modeled vertical profiles of the normalized standard deviation of pressure for the top 8 m of the model domain during the June 14-20, 2012 study period. Although difficult to tell from the high frequencies (Figure 11c), this figure indicates that, regardless of the forcing frequency, within the top 1 m or so the surface pressure attenuates with depth more strongly with the nonlinear models than do either the Linear model or COM approach. This difference in near-surface pressure gradients is made more obvious in Figure 12, which shows the modeled vertical profiles of $\sigma_v(z)$ for the top 8 m of the model domain during the June 14-20, 2012 study period. All profiles in this figure show a maximum at approximately 1.4 m, which corresponds to the maximum in the MEF soil permeability of approximately two orders of magnitude greater than the very-near surface permeability (Appendix B).

Figure 11c also offers an insight into the COM approach. Although not shown here, within the top meter of the domain the nonlinear $D_{p,high} \approx 0.9$ m, whereas the linear $D_{p,high} \approx 2$ m. But as shown in Table 1, σ_{vp} for $D_{p,high} = 2$ m (linear model) agrees more closely with the nonlinear estimate of σ_{vp} than it does with the linear estimate and vice versa for $D_{p,high} = 0.9$ m (nonlinear model). In other words, the ability of the COM to distinguish between the linear and nonlinear models, or to offer any insights for preferring one type of model over the other, is not only lost at high frequencies, it yields inferences that are completely opposite of model-based expectations. This same reversal occurs with the COM with the mid- and low frequencies, but σ_{vp} is much less sensitive to variations (or uncertainties) in $D_{p,mid}$ or $D_{p,low}$, so the COM resembles the linear model more than the nonlinear models.

For those cases that do not include soil heat and moisture dynamics these last Figures 10 and 11 are elaborations of the results summarized in Table 1 and Equation (22). But the differences between the linear and nonlinear approaches is more complicated when heat and moisture effects are included, e.g., Figure 13, which shows that heat and moisture dynamics have very little impact on the Linear model, but for the two nonlinear models its impact on the vertical structure of the pressure gradient and the advective velocity are more significant. Both the surface gradient, or equivalently the surface velocities – Table 1, rows v_{pM*} and v_{pA*} , June and October study periods – and the general overall gradient (compare Figures 11, 12 and 13) suggest that the nonlinear models are fairly sensitive to heat and moisture dynamics. This may not be too surprising given that these are nonlinear hyperbolic models, e.g., Hinch (2020) and that $|\partial p_\beta / \partial z| \ll |\Lambda_z|$ (Equations (14) and (15)), which changes the nature of the non-linearity of these hyperbolic models. Present results suggests that heat and moisture dynamics have the potential to impact the nonlinear models’ solutions, particularly in the upper meter or so of the soil profile. But the degree of sensitivity is more than (at least) these authors were expecting. It is difficult to generalize beyond this undistinguished conclusion concerning the nonlinear models’ sensitivity. In part, this is because for the June study period v_{pM*} and v_{pA*} (Table 1) are more-or-less unsurprising and in agreement with expectations, whereas for the October study period they are one to two orders of magnitude greater than might have been expected. One possible explanation might be that the nonlinear models are unstable and, therefore, their solutions are physically unrealistic. The “jaggedness” (discontinuities) of the nonlinear models’ vertical profiles shown in Figure 13 might support this notion. Furthermore, the authors’ experience suggests that once model velocities begin to approach or exceed about 10 mms^{-1} (or $10^4 \mu\text{ms}^{-1}$) these models can become unstable. But decreasing the vertical spacing (from the current 0.10 m) did not produce any clear insights into these potential model instabilities or eliminate the discontinuities. Beyond this somewhat obvious conclusion that the nonlinear models’ are relatively sen-

954 sensitive to heat and moisture effects, present results offer only that more numerical and
955 observational investigations seem warranted.

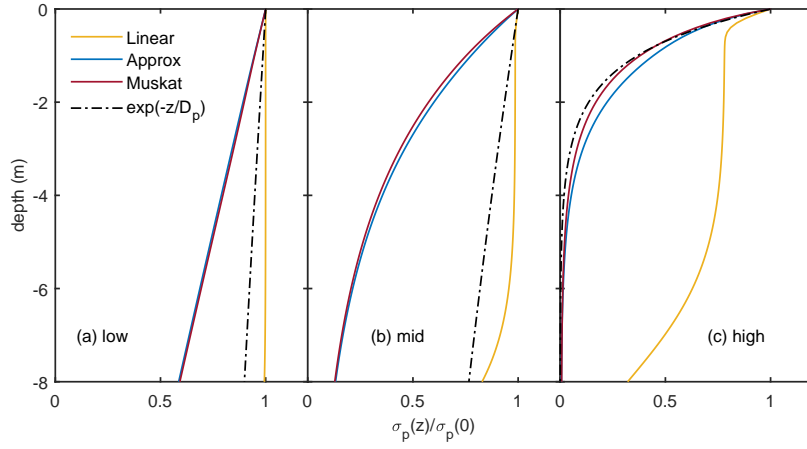


Figure 11. Modeled vertical profiles of the normalized standard deviation of pressure for the top 8 m of the model domain during the June 14-20, 2012 study period. The COM approach is identified by the expression $\exp(-z/D_p)$, where $D_p = 75$ m for the low frequencies, for mid frequencies $D_p = 30$ m, and D_p for the high frequencies is 1 m.

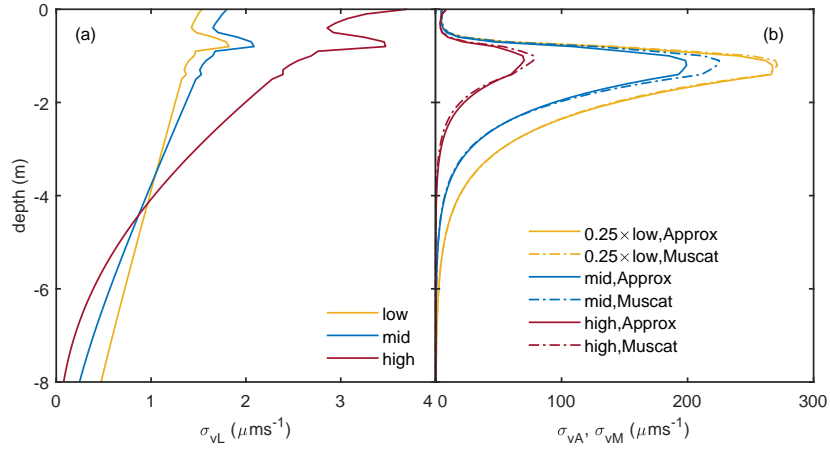


Figure 12. Modeled vertical profiles of the standard deviation of advective velocities for the top 8 m of the model domain during the June 14-20, 2012 study period. Panel (a) shows the low frequencies, (b) the mid frequencies and (c) for the high frequencies. All profiles show a maximum at approximately 1.4 m, which corresponds to the maximum in the MEF soil permeability of $k(-1.4) \approx 250 \times 10^{-12} \text{ m}^2 \approx 40 \times k(0)$. The second letter of each subscript refers to the model: ‘L’ is the linear model, ‘A’ is the approximate model (solid lines) and ‘M’ refers to the Muskat model (dash-dot lines).

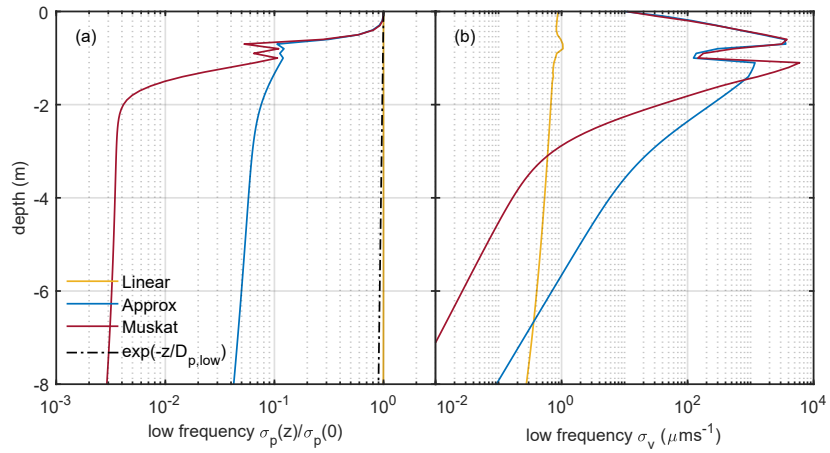


Figure 13. Low frequency (June 2012) modeled profiles in the top 8 m of the model domain with heat and moisture dynamics included (i.e., Equations (13), (14) and (15)). The COM approach is identified by the expression $\exp(-z/D_p)$, where $D_p = 75$ m for the low frequencies. Panel (a) shows the modeled vertical profiles of the normalized standard deviation of pressure and panel (b) the standard deviation of advective velocities.

5 Summary and Conclusions

(1) Model Comparisons: This study begins with a review of the physical fundamentals of two different categories of models used to describe pressure-induced advective (i.e., non-diffusive) gas flow in permeable media at the earth's surface. Both types of models have been used for decades to describe pressure pumping, but mathematically they are very different, with one model characterized as linear parabolic (Buckingham, 1904) and the other two, slightly different, models as nonlinear hyperbolic (Muskat, 1937; Kidder, 1957; J. W. Massmann, 1989). The linear model results from assuming that the flow field is compressible (i.e., $\nabla \bullet v \neq 0$) and the nonlinear models both assume that the flow field is incompressible (i.e., $\nabla \bullet v = 0$). The numerical results, summarized by Table 1 and Figure 10, were (mostly) anticipated by a linear analysis of the model equations (Section 2.2.2 and Equation (16)) and show that the nonlinear models will always yield advective velocities that are similar to one another but always greater than those of the linear model by approximately an order of magnitude and that the difference between these two types of models is greatest for low frequency forcings (i.e., phenomena with periods ≥ 5 hours). In fact the differences were great enough to suggest that low frequency advective motions induced by pressure changes (for soils with permeability similar to those at MEF) is small enough in the Linear model to be neglected, contrary to expectations. On the other hand, low frequency advective motion within snowpacks is likely to be significant because the permeability of snowpacks is often two or more orders of magnitude greater than it is for MEF soils, i.e., $k_{snowpack} = (1 - 100)10^{-10}$ m² (e.g., Sommerfeld and Rocchio (1993); Albert and Shultz (2002)). For mid (periods between 0.5 and 5 hours) and high (periods between 1 s and 5 hours) frequencies the model differences are less, but are still significant. The vertical profiles of pressure and velocities were also very different with the nonlinear models associated with velocities of much greater magnitude, but more strongly attenuated, within the top 5 m of the soil than the Linear model. Overall, model-based numerical estimates of pressure induced trace gas exchange between the atmosphere and soils and snowpacks is strongly model dependent and, therefore, any quantitative results are potentially biased or incorrect.

Because the conservation of mass (COM) approach, Equation (19), is independent of the compressible/incompressible flow assumption it was originally hoped that it would provide some ability to discriminate (or choose) between the linear and nonlinear models. But this was not really the case, despite its apparent congruence with the Linear model, Equation (7). There are two principal reasons for this. First for high frequencies, using the best estimate of the Linear model's attenuation depth, D_p (the key input parameter of the COM), yielded an estimate of v_p that agreed more closely with nonlinear models and vice versa for the nonlinear models' best estimate of D_p . Second, although for low frequency surface forcing the COM agreed very closely with the Linear model, these velocities were so low compared to all other velocities as to suggest that the low frequency forcing is negligible, as mentioned in the previous paragraph.

(2) Heat and Moisture Dynamics: Changes in temperature and moisture can influence the pressure within the soil pore spaces (Equations (13), (14) and (15)) especially during the daily cycle (i.e., low frequencies). The Linear model showed very little sensitivity to these dynamics. Nonetheless, there was some suggestion that the advective velocity associated with soil moisture was surprisingly higher than what was expected, especially during rain events. The nonlinear models were far more sensitive to heat and moisture dynamics than the Linear model. In fact, these additional forcings enhanced the (already significant) nonlinear low frequency pressure-only advective velocities by an order of magnitude, which again was unanticipated. If this result could be observationally verified, it would suggest that interplay of the daily cycles of atmospheric forcing and soil heating is a significant driver of soil evaporation (from relatively moist soils, of course).

1008 (3) Mid and High Frequency Forcing by Mesoscale Atmospheric Events: Both the
 1009 linear and nonlinear models are unambiguous about the importance of mid and high fre-
 1010 quency forcing to soil gas transport, with the linear model even suggesting that the trans-
 1011 port at these frequencies are the dominant forcing frequencies. A novel contribution of
 1012 the present study is the recognition that significant gas transport in soils is associated
 1013 with and enhanced by mid-frequency mesoscale atmospheric phenomena, such as inertia-
 1014 gravity waves and solitons (Figures 7 and 9). These phenomena, often generated by larger
 1015 scale atmospheric events like thunderstorms and frontal systems, are important in their
 1016 own right as forcings for transport. But they also intensify the diurnal cycle of turbu-
 1017 lence, itself the key, high frequency, driver of soil gas transport. Thus further research
 1018 into pressure pumping in soils and snowpacks should be aware of the significance of the
 1019 mid-frequency forcings and their strong coupling to the high frequency forcing.

1020 (4) A Summation: In the simplest terms and all other things being equal, the non-
 1021 linear models portray the action of the atmosphere on soil gas transport as significantly
 1022 more dynamic and consequential than the linear models. Given the increasing need for
 1023 understanding of climate change's influence on the intensification of hydrologic events,
 1024 such as droughts and rainfall, on soil evaporation and respiration, it seems worthwhile
 1025 to be aware of (and maybe resolve) this difference.

1026 Appendix A Nonlinear models and the Burgers Equation

1027 This appendix shows how two different models of pressure pumping, the Muskat
 1028 (incompressible flow) model and the weakly nonlinear form of the parabolic (or compress-
 1029 ible flow) model, are related to Burgers Equation. Following the notation of the main
 1030 text the one-dimensional Muskat model is

$$1031 \frac{\partial p_\beta}{\partial t} - \frac{k}{(\eta - \theta)\mu} \left(\frac{\partial p_\beta}{\partial z} \right)^2 = 0 \quad (A1)$$

1032 and the one-dimensional weakly nonlinear form of the parabolic model is

$$1033 \frac{\partial p_\beta}{\partial t} - \frac{k}{(\eta - \theta)\mu} \left(\frac{\partial p_\beta}{\partial z} \right)^2 - P \frac{\partial}{\partial z} \left(\frac{k}{(\eta - \theta)\mu} \frac{\partial p_\beta}{\partial z} \right) = 0 \quad (A2)$$

1034 In terms of the Darcy velocity, $v_p = -k/((\eta - \theta)\mu)(\partial p_\beta/\partial z)$, and the pressure diffu-
 1035 sivity, $\kappa = Pk/((\eta - \theta)\mu)$, (A1) can be expressed as

$$1036 \frac{\kappa}{P} \frac{\partial p_\beta}{\partial t} - v_p^2 = 0 \quad (A3)$$

1037 and (A2) as

$$1038 \frac{\kappa}{P} \frac{\partial p_\beta}{\partial t} - v_p^2 + \kappa \frac{\partial v_p}{\partial z} = 0 \quad (A4)$$

1039 Assuming that the temporal and spatial differentiation operators commute, differ-
 1040 entiate the last two expressions with respect to z , then employ Darcy's law again (with
 1041 the further assumption assume that k is not a function of time). This transforms (A1)
 1042 into the inviscid form of Burgers Equation,

$$1043 \frac{\partial v_p}{\partial t} + 2v_p \frac{\partial v_p}{\partial z} = 0 \quad (A5)$$

1044 and (A2) into a viscid form of Burgers Equation,

$$1045 \quad \frac{\partial v_p}{\partial t} + 2v_p \frac{\partial v_p}{\partial z} - \frac{\partial}{\partial z} \left(\kappa \frac{\partial v_p}{\partial z} \right) = 0 \quad (\text{A6})$$

1046 It may be more appropriate to term Equation (A6) a pseudo-Burgers Equation,
 1047 because unlike Burgers Equation, the diffusive term $\partial/\partial z (\kappa \partial v_p/\partial z)$ is much greater in
 1048 magnitude than the nonlinear term $2v_p \partial v_p/\partial z$ as shown above in the section 2.2.1 of the
 1049 manuscript. Nevertheless, the standard way of solving viscid Burgers Equation, i.e., the
 1050 Cole-Hopf transformation (Cole (1951); Hopf (1950)), can also be used to solve (A6) and
 1051 therefore, (A2) as well. The analytical solution to (A2) is developed as follows:

1052 Define a function $\widehat{p} = \widehat{p}(z, t)$ such that

$$1053 \quad \frac{1}{\widehat{p}} \frac{\partial \widehat{p}}{\partial z} = \frac{1}{P} \frac{\partial p}{\partial z} \quad (\text{A7})$$

1054 After integrating this last expression with respect to z yields:

$$1055 \quad \ln(\widehat{p}(z, t)) = \frac{p(z, t)}{P} + \widehat{P}(t) \quad (\text{A8})$$

1056 where $\widehat{P}(t)$ (*dimensionless*) is “the constant of integration”, which in this case can be
 1057 a function of time, t , and is related to the boundary conditions. Next simply apply Equa-
 1058 tion (A7) to Equation (A2) to obtain

$$1059 \quad \frac{\partial \widehat{p}}{\partial t} - \frac{\partial}{\partial z} \left(\kappa \frac{\partial \widehat{p}}{\partial z} \right) - \widehat{p} \widehat{P}'(t) = 0 \quad (\text{A9})$$

1060 where (i) $\widehat{P}'(t) = d\widehat{P}/dt$ is the first derivative of \widehat{P} with respect to t and (ii) (A9) is
 1061 subject to the boundary condition: $\ln(\widehat{p}(0, t)) = p(0, t)/P + \widehat{P}(t)$ or $\widehat{p}(0, t) = \widehat{P}_*(t) \exp(p(0, t)/P)$,
 1062 where $\widehat{P}_*(t) = \exp(\widehat{P}(t))$.

1063 By demonstrating the connection between Burgers Equation and (A1) and (A2)
 1064 above this Appendix should make numerical and mathematical methods developed for
 1065 solving Burgers Equation (e.g., Kochina (1961); Platzman (1964); Benton and Platzman
 1066 (1972); Kadalbajoo and Awasthi (2006); Kurt et al. (2015); Çenesiz et al. (2017); Mo-
 1067 hamed (2019)) available for obtaining $p(z, t)$ from either the compressible or incompress-
 1068 ible model of pressure pumping in soils.

1069 Appendix B Observed 1 m vertical profiles of ρ_s and k_u at MEF

Table B1. Vertical profile of MEF soil bulk density, ρ_s

Soil Depth (m)	Bulk Density (Mgm ⁻³)
0.0 - 0.1	1.20
0.1 - 0.2	1.13
0.2 - 0.3	1.07
0.3 - 0.4	1.02
0.4 - 0.5	1.08
0.5 - 0.6	1.26
0.6 - 0.7	1.48
0.7 - 0.8	1.58
0.8 - 0.9	1.73
0.9 - 1.0	1.63

Table B2. Vertical profile of MEF soil permeability obtained for the top 1 m only. The samples were obtained with a sample tube 0.05 m in length. The vertical sample was obtained with the sample tube inserted vertically into the soil. The horizontal sample was obtained with the sample tube inserted horizontally every 0.05 m starting at 0.025 m.

Soil Depth (m)	Vertical Sample $k(z)$ (10^{-12} m ²)	Horizontal Sample $k(z)$ (10^{-12} m ²)
0.00 - 0.05	11	12
0.05 - 0.10	4.5	13
0.10 - 0.15	1.0	4.9
0.15 - 0.20	5.6	2.9
0.20 - 0.25	3.1	2.4
0.25 - 0.30	1.7	3.0
0.30 - 0.35	1.3	2.8
0.35 - 0.40	1.0	3.7
0.40 - 0.45	1.7	2.4
0.45 - 0.50	1.2	2.6
0.50 - 0.55	2.1	2.1
0.55 - 0.60	2.7	74
0.60 - 0.65	72	8.4
0.65 - 0.70	13	19
0.70 - 0.75	52	12
0.75 - 0.80	25	1.6
0.80 - 0.85	140	120
0.85 - 0.90	120	200
0.90 - 0.95	110	43
0.95 - 1.00	250	28

1070

Appendix C The pressure sensor: calibration and data quality

1071

1072

1073

1074

1075

1076

1077

1078

1079

1080

1081

1082

1083

1084

1085

1086

1087

1088

1089

1090

1091

1092

1093

Soil pressure was measured in a single pit at 0, 10, 20, and 50 cm. The tube inlet for pressure at each of these depths used a stainless steel fitting (Swagelok, Solon, OH) with one end covered with a porous stainless steel mesh, but otherwise open to the soil and the other end connected to a high-precision/limited-range differential pressure transducer (226A Baratron differential capacitance manometer, MKS Instruments, Andover, MA) via Dekoron tubing (0.95 cm O.D., 0.64 cm I.D). The tubing was buried about 0.5 m deep. The other side of the differential pressure transducer was connected to one end of an ≈ 1 L stainless steel cylinder used to provide a relatively constant reference pressure, P_{ref} . The other end of the reference cylinder was connected to a solenoid (Skinner valve, model 71215SN2MN00N0, Parker, New Britain, CT) that was periodically opened and closed to refresh the pressure within the reference cylinder whenever the pressure transducer drifted out of range; the cylinder attached to the 50 cm inlet did not have a solenoid valve and instead was plugged. The transducers and reference volumes were placed in a control box that was buried about 1 m under the soil. A CR3000 datalogger (Campbell Scientific), located in a separate enclosure placed on the soil surface, measured and recorded each differential pressure transducer at 1 Hz, and whenever the data for an inlet was out of range (i.e., > 500 Pa or < -500 Pa) the datalogger opened the corresponding solenoid for 2 seconds before closing it. The datalogger also recorded the temperature inside the buried control box with a thermistor (Temp 107 probe, Campbell Scientific) and the temperature within the 50 cm reference cylinder, T_{ref} ; instead of a solenoid on this cylinder there was a plug that encased and sealed a platinum resistance thermometer within it (Omega 100-ohm platinum-RTD, model RTD-810, with a Omega signal conditioning module, model OM5IP4-N100-C, Omega Engineering). This methodology pro-

1094 vided differential pressure measurements between the air within the soil and the air within
 1095 the interior of a rigid reference volume with an arbitrary, but nearly constant, number
 1096 of molecules (i.e., the pressure captured within the reference cylinder at the time of the
 1097 last opening/closing of the solenoid valve adjusted for temperature changes within the
 1098 cylinder as well as leaks, such as and molecular exchange across the pressure sensor’s di-
 1099 aphragm).

1100 The original data contained subsets of differential pressure signals whose pressures
 1101 inside their reference cylinders were arbitrary and varied slowly over time; these signals
 1102 required stitching to create a coherent dataset for analysis. First, obvious data outliers
 1103 were identified and removed based on their 5-minute averages or standard deviations.
 1104 Next, a Bayesian statistical analysis was used to stitch the signals together. The pres-
 1105 sure signals between the opening/closing of the solenoid valves were bundled into time
 1106 blocks, with each time block assigned a Bayesian process parameter describing the cylin-
 1107 der pressure, P_{ref} . The Bayesian statistical analysis predicted the corrected soil pres-
 1108 sure, $P_s = P_{s,raw} + P_{ref}$; where the correction term is $P_{ref} = P_{ref,init} + c_{\rho,T} * \rho_{a,ref} * T_{ref} * 287.058 - c_1 t - c_2 t^2 - c_3 t^3$ and t (minutes) is time, $P_{ref,init}$, $c_{\rho,T}$, c_1 , c_2 , and c_3
 1109 are empirical fitting parameters with posterior probability distributions and $\rho_{a,ref}$ is cal-
 1110 culated from the ideal gas law using P_a (ambient air pressure, described below) and T_{ref} .
 1111 Direct measurements of the cylinder temperatures were used, but if missing, the soil tem-
 1112 perature at 50 cm depth was substituted. The Bayesian analysis estimates the most likely
 1113 combination of initial reference cell pressure, temperature drift, and time drift between
 1114 every purging of the reference cell in order make the four soil pressure signals match each
 1115 other as well as the match P_a . Finally, P_{ref} was calculated for each five-minute period,
 1116 and then interpolated to 1 Hz and added to the raw pressure data, $P_{s,raw}$. This method-
 1117 ology, which treats P_a as a standard, yields an average absolute accuracy for the soil pres-
 1118 sure sensors of $P_a \pm 17$ Pa, while the difference in precision of the standard deviation be-
 1119 tween the four soil pressure sensors is ± 1 Pa. Therefore, soil air pressure differences in
 1120 the vertical can typically be measured within ± 1 Pa while retaining low-frequency trends
 1121 within each pressure signal.
 1122

1123 The ambient pressure is necessary to allow an accurate reconstruction of the soil
 1124 pressure profiles over time. The goal was to allow the Bayesian analysis to slowly adjust
 1125 the reference cylinder pressures so that each block of time would accurately reflect the
 1126 absolute pressure observed at the field site. From 8 July 2009 until 28 September 2012
 1127 the absolute ambient pressure was taken from at the National Center for Atmospheric
 1128 Research (NCAR) Manitou Experimental Forest Observatory, P_{NCAR} (*BEACHON 5 minute*
 1129 *ISFS data, not tilt corrected.*, n.d.). After 28 September 2012 there were no absolute am-
 1130 bient pressure measurements recorded at MEF; instead, an adjusted version of the am-
 1131 bient pressure at the Niwot Ridge AmeriFlux site (P_{NR1}) 110 km north-northwest (Blanken
 1132 et al., 1998) was used. This was done by first developing a relationship between P_{NR1}
 1133 and P_{NCAR} during the overlap period between 8 July 2009 and 28 September 2012. The
 1134 P_{NR1} data were LOESS filtered with a 2-day window and then used as an independent
 1135 variable to predict the NCAR pressure data from the equation $P_{NCAR} = a P_{NR1} + b +$
 1136 $c \sin(2\pi t / 365.25 + d)$ where a , b , c , and d are empirical fitting parameters and t (days)
 1137 is time, an independent variable. For both the NCAR and adjusted Niwot Data, the mean
 1138 value of 76.283 kPa at MEF was removed from the datasets. The Bayesian parameters
 1139 were adjusted such that the analysis tried to match the four soil pressure sensors with
 1140 the same precision to each other as P_{NCAR} , but it allowed the matching to P_{NR1} to be
 1141 less rigorous because this dataset is considered a surrogate for the actual pressures at
 1142 MEF.

1143 Acknowledgments

1144 The authors wish to thank Dr Al Bedard for his thoughts and insights regarding atmo-
 1145 spheric gravity waves, lee waves and infrasound, Dr Ned Patton for his making the NCAR

1146 data available to us, and Dr Shane Mayor for pointing out the UCAR weather data archive
1147 at <https://www2.mmm.ucar.edu/imagearchive/>.

1148 Data Availability Statement

1149 The computer code used in this study was developed using MatLab version 2017b
1150 and is publicly available along with any output data at the Forest Service Research Data
1151 Archive <https://doi.org/10.2737/RDS-2021-XXXX>. It is also freely available from the
1152 lead author.

1153 References

- 1154 Albert, M. R. (2002). Effects of snow and firn ventilation on sublimation rates. *Annals of*
1155 *Glaciology*, *35*, 52–56. <https://doi.org/10.3189/172756402781817194>.
- 1156 Albert, M. R., & McGilvary, W. R. (1992). Thermal effects due to air flow and vapor
1157 transport in dry snow. *Journal of Glaciology*, *38*(129), 273–281.
1158 <https://doi.org/10.3189/S0022143000003683>.
- 1159 Albert, M. R., & Shultz, E. F. (2002). Snow and firn properties and air–snow transport
1160 processes at Summit, Greenland. *Atmospheric Environment*, *36*(15-16), 2789–2797.
1161 [https://doi.org/10.1016/S1352-2310\(02\)00119-X](https://doi.org/10.1016/S1352-2310(02)00119-X).
- 1162 Bartelt, P., Buser, O., & Sokratov, S. A. (2004). A nonequilibrium treatment of heat and
1163 mass transfer in alpine snowcovers. *Cold Regions Science and Technology*, *39*,
1164 219–242. <https://doi.org/10.1071/SR9680031>.
- 1165 *BEACHON 5 minute ISFS data, not tilt corrected.* (n.d.). (NCAR/EOL Data Archive:
1166 <https://data.eol.ucar.edu/dataset/183867>)
- 1167 Bedard, A. J. (1998). Recent advances in infrasonic and near infrasonic atmospheric
1168 sounding and imaging. In *Fourth international workshop on radar polarimetry*
1169 *Nantes, 13–17 July 1998* (pp. 269–). France: Laboratoire systèmes électroniques &
1170 informatiques. ISBN 2-909805-09-3.
- 1171 Bedard, A. J. (2005). Low-frequency atmospheric acoustic energy associated with vortices
1172 produced by thunderstorms. *Monthly Weather Review*, *133*(1), 241–263.
1173 <https://doi.org/10.1175/MWR-2851.1>.
- 1174 Benton, E. R., & Platzman, G. W. (1972). A table of solutions of the one-dimensional
1175 Burgers equation. *Quarterly of Applied Mathematics*, *30*(2), 195–212.
1176 <https://doi.org/10.1090/qam/306736>.
- 1177 Berryman, E. M., Frank, J. M., Massman, W. J., & Ryan, M. G. (2018). Using a
1178 Bayesian framework to account for advection in seven years of snowpack CO₂ fluxes
1179 in a mortality-impacted subalpine forest. *Agricultural and Forest Meteorology*, *249*,
1180 420–433. <https://doi.org/10.1016/j.agrformet.2017.11.004>.
- 1181 Blanken, P. D., Monson, R. K., Burns, S. P., Bowling, D. R., & Turnispeed, A. A. (1998).
1182 *AmeriFlux US-NR1 Niwot Ridge Forest (LTER NWT1)*. (AmeriFlux Data Archive:
1183 <https://doi.org/10.17190/AMF/1246088>)
- 1184 Bourret, S. M., Kwicklis, E. M., Miller, T. A., & Stauffer, P. H. (2018). Evaluating the
1185 importance of barometric pumping for subsurface gas transport near an
1186 underground nuclear test site. *Vadose Zone Journal*, *18*, 180134.
1187 <https://doi.org/10.2136/vzj2018.07.0134>.
- 1188 Bowling, D. R., & Massman, W. J. (2011). Persistent wind-induced enhancement of
1189 diffusive CO₂ fluxes in a mountain forest snowpack. *Journal Geophysical Research*,
1190 *116*, G04006. <https://doi.org/10.1029/2011JG001722>.
- 1191 Brooks, J. R., Meinzer, F. C., Coulombe, R., & Gregg, J. (2002). Hydraulic redistribution
1192 of soil water during summer drought in two contrasting pacific northwest coniferous
1193 forests. *Tree Physiology*, *22*, 1107–1117.
1194 <https://doi.org/10.1093/treephys/22.15-16.1107>.
- 1195 Buckingham, E. (1904). *Contributions to our knowledge of the aeration of soils.* (Bureau
1196 of Soils – Bulletin No. 25). Government Printing Office, Washington, D. C.: US
1197 Department of Agriculture.

- 1198 Campbell, G. S., & Norman, J. M. (1998). *An Introduction to Environmental Biophysics*.
 1199 (Second ed.). New York, NY, USA: Springer-Verlag New York, Inc. (ISBN
 1200 0-387-94937-2)
- 1201 Çenesiz, Y., Baleanu, D., Kurt, A., & Tasbozan, O. (2017). New exact solutions of
 1202 Burgers type equations with conformable derivative. *Waves in Random and*
 1203 *Complex Media*, 27(1), 103–116. <https://doi.org/10.1080/17455030.2016.1205237>.
- 1204 Chen, C., Thomas, D. M., & Green, R. E. (1995). Modeling of radon transport in
 1205 unsaturated soil. *Journal of Geophysical Research - Solid Earth*, 100(B8),
 1206 15517–15525. <https://doi.org/10.1029/2000WR900128>.
- 1207 Christie, D. R. (1989). Long nonlinear waves in the lower atmosphere. *Journal of the*
 1208 *Atmospheric Sciences*, 46(11), 1462–1491.
 1209 [https://doi.org/10.1175/1520-0469\(1989\)046<1462:LNWITL>2.0.CO;2](https://doi.org/10.1175/1520-0469(1989)046<1462:LNWITL>2.0.CO;2).
- 1210 Clarke, G. K. C., Fisher, D. A., & Waddington, E. D. (1987). Wind pumping: A
 1211 potentially significant heat source in ice sheets. In E. D. Waddington & J. S. Walder
 1212 (Eds.), *International Association of Hydrological Sciences 170 (Symposium at*
 1213 *Vancouver 1987) – The Physical Basis of Ice Sheet Modelling*. (pp. 169–180). IAHS,
 1214 UKCEH Wallingford, Oxfordshire OX10 8BB, UK: International Association of
 1215 Hydrological Sciences. ISBN 0-947571-36-1.
- 1216 Clements, W. E., & Wilkening, M. H. (1974). Atmospheric pressure effects on ^{222}Rn
 1217 transport across the earth-air interface. *Journal of Geophysical Research*, 79(33),
 1218 5025–5029. <https://doi.org/10.1029/JC079i033p05025>.
- 1219 Cole, J. (1951). On a quasi-linear parabolic equation occurring in aerodynamics.
 1220 *Quarterly of Applied Mathematics*, 9(3), 225–236.
 1221 <https://www.jstor.org/stable/43633894>.
- 1222 Czepiel, P. M., Shorter, J. H., Mosher, B., Allwine, E., McManus, J. B., Harriss, R. C., et
 1223 al. (2003). The influence of atmospheric pressure on landfill methane emissions.
 1224 *Waste Management*, 23, 593–598. [https://doi.org/d10.1016/S0956-053X\(03\)00103-X](https://doi.org/d10.1016/S0956-053X(03)00103-X).
- 1225 Depcik, C., & Loya, S. (2012). Dynamically incompressible flow. In S. A. Jones (Ed.),
 1226 *Advanced methods for practical applications in fluid mechanics* (pp. 71–98). Rijeka,
 1227 Croatia: InTech. ISBN: 978-953-51-0241-0; Available from:
 1228 [http://www.intechopen.com/books/advanced-methods-for-practical-applications-in-](http://www.intechopen.com/books/advanced-methods-for-practical-applications-in-fluidmechanics/dynamically-incompressible-flow)
 1229 [fluidmechanics/dynamically-incompressible-flow](http://www.intechopen.com/books/advanced-methods-for-practical-applications-in-fluidmechanics/dynamically-incompressible-flow).
- 1230 Doviak, R. J., & Ge, R. (1984). An atmospheric solitary gust observed with a Doppler
 1231 radar, a tall tower and a surface network. *Journal of the Atmospheric Sciences*,
 1232 41(17), 2559–2573.
 1233 [https://doi.org/10.1175/1520-0469\(1984\)041<2559:AASGOW>2.0.CO;2](https://doi.org/10.1175/1520-0469(1984)041<2559:AASGOW>2.0.CO;2).
- 1234 Drake, S. A., Selker, J. S., & Higgins, C. W. (2019). Pressure-driven vapor exchange with
 1235 surface snow. *Frontiers in Earth Science*, 7, 201.
 1236 <https://doi.org/10.3389/feart.2019.00201>.
- 1237 Dubrovin, L. I. (1961). Air currents in the snow and firn layer of Lazarev ice shelf.
 1238 *Sovetskaia antarkticheskaia ekspeditsiia. Informatsionnyi biulleten.*, 26, 13–14.
 1239 English translation in: Soviet Antarctic Expedition, Information Bulletin. Vol. 3,
 1240 Amsterdam, Elsevier, 1965, p.218–219.
 1241 <https://www.coldregions.org/vufind/Record/139194>.
- 1242 Einaudi, F., Bedard, A. J., & Finnigan, J. J. (1989). A climatology of gravity waves and
 1243 other coherent disturbances at the Boulder Atmospheric Observatory during
 1244 March/April 1984. *Journal of the Atmospheric Sciences*, 46(3), 303–329.
 1245 [https://doi.org/10.1175/1520-0469\(1989\)046<0303:ACOGWA>2.0.CO;2](https://doi.org/10.1175/1520-0469(1989)046<0303:ACOGWA>2.0.CO;2).
- 1246 Elberling, B., Larsen, F., Christensen, S., & Postma, D. (1998). Gas transport in a
 1247 confined unsaturated zone during atmospheric pressure cycles. *Water Resources*
 1248 *Research*, 34(11), 2855–2862. <https://doi.org/10.1029/98WR02037>.
- 1249 Etiope, G., & Martinelli, G. (2002). Migration of carrier and trace gases in the geosphere:
 1250 an overview. *Physics of the Earth and Planetary Interiors*, 129(3-4), 185–204.
 1251 [https://doi.org/10.1016/S0031-9201\(01\)00292-8](https://doi.org/10.1016/S0031-9201(01)00292-8).

- 1252 Fain, X., Helmig, D., Hueber, J., Obrist, D., & Williams, M. W. (2013). Mercury
1253 dynamics in the Rocky Mountain, Colorado, snowpack. *Biogeosciences*, *10*(6),
1254 3793–3807. <https://doi.org/10.5194/bg-10-3793-2013>.
- 1255 Falta, R. W., Javandel, I., Pruess, K., & Witherspoon, P. A. (1989). Density-driven flow
1256 of gas in the unsaturated zone due to the evaporation of volatile organic compounds.
1257 *Water Resources Research*, *25*(10), 2159–2169.
1258 <https://doi.org/10.1029/WR025i10p02159>.
- 1259 Finnigan, J. J. (1979). Turbulence in waving wheat I. Mean statistics and honami.
1260 *Boundary-Layer Meteorology*, *16*(2), 181–211. <https://doi.org/10.1007/BF02350511>.
- 1261 Forde, O. N., Cahill, A. G., Beckie, R. D., & Mayer, K. U. (2019). Barometric-pumping
1262 controls fugitive gas emissions from a vadose zone natural gas release. *Scientific*
1263 *Reports*, *9*, 14080. <https://doi.org/10.1038/s41598-019-50426-3>.
- 1264 Frank, J. M., & Massman, W. J. (2020). *2008-2014 Soil temperature, thermal*
1265 *conductivity, water content, CO₂, and pressure at the Manitou Experimental Forest,*
1266 *Colorado during the Bio-hydro-atmosphere interactions of Energy, Aerosols, Carbon,*
1267 *H₂O, Organics & Nitrogen (BEACHON) study.* Rocky Mountain Research Station,
1268 Fort Collins, Colorado. (Forest Service Research Data Archive:
1269 <https://doi.org/10.2737/RDS-2020-0061>)
- 1270 Fritts, D. C., & Alexander, M. J. (2003). Gravity wave dynamics and effects in the
1271 middle atmosphere. *Reviews of Geophysics*, *41*(1), 1003.
1272 <https://doi.org/10.1029/2001RG000106>.
- 1273 Fukuda, H. (1955). Air and vapor movement in soil due to wind. *Soil Science*, *79*,
1274 249–256. <https://doi.org/10.1097/00010694-195504000-00002>.
- 1275 Goncharov, V. P., & Matveyev, A. K. (1982). Observations of nonlinear waves on an
1276 atmospheric inversion. *Izvestiya, Atmospheric and Oceanic Physics*, *18*(1), 61–64.
1277 <https://www.researchgate.net/publication/259382702>.
- 1278 Gray, J. M. N. T., & Morland, L. W. (1994). A dry snowpack model. *Cold Regions*
1279 *Science and Technology*, *22*, 135–148.
1280 [https://doi.org/10.1016/0165-232X\(94\)90025-6](https://doi.org/10.1016/0165-232X(94)90025-6).
- 1281 Grifoll, J., Gastó, J. M., & Cohen, Y. (2005). Non-isothermal soil water transport and
1282 evaporation. *Advances in Water Resources*, *28*(11), 1254–1266.
1283 <https://doi.org/10.1016/j.advwatres.2005.04.008>.
- 1284 Grivet-Talocia, S., Einaudi, F., Clark, W. L., Dennett, R. D., Nastrom, G. D., &
1285 VanZandt, T. E. (1999). A 4-yr climatology of pressure disturbances using a
1286 barometer network in central Illinois. *Monthly weather review*, *127*(7), 1613–1629.
1287 [https://doi.org/10.1175/1520-0493\(1999\)127<1613:AYCOPD>2.0.CO;2](https://doi.org/10.1175/1520-0493(1999)127<1613:AYCOPD>2.0.CO;2).
- 1288 Hauf, T., Finke, U., Neisser, J., Bull, G., & Stangenberg, J.-G. (1996). A ground-based
1289 network for atmospheric pressure fluctuations. *Journal of Atmospheric and Oceanic*
1290 *Technology*, *13*(5), 1001–1023.
1291 [https://doi.org/10.1175/1520-0426\(1996\)013<1001:AGBNFA>2.0.CO;2](https://doi.org/10.1175/1520-0426(1996)013<1001:AGBNFA>2.0.CO;2).
- 1292 Hinch, E. J. (2020). *Think Before You Compute.* Cambridge CB2 8BS, UK: Cambridge
1293 University Press. (ISBN 978-1-108-78999-8)
- 1294 Hinkle, M. E. (1994). Environmental conditions affecting concentrations of He, CO₂, O₂
1295 and N₂ in soil gases. *Applied Geochemistry*, *9*(1), 53–63.
1296 [https://doi.org/10.1016/0883-2927\(94\)90052-3](https://doi.org/10.1016/0883-2927(94)90052-3).
- 1297 Hopf, E. (1950). The partial differential equation $u_t + uu_x = \mu u_{xx}$. *Communications on*
1298 *Pure and Applied Mathematics*, *3*(3), 201–230. <https://doi.org/10.1002/cpa.3160030302>.
- 1299 Hu, J., Yang, G., Hegedús, M., Iwaoka, K., Hosoda, M., & Tokonami, S. (2018).
1300 Numerical modeling of the sources and behaviors of ²²²Rn, ²²⁰Rn and their
1301 progenies in the indoor environment – A review. *Journal of Environmental*
1302 *Radioactivity*, *189*, 40–47. <https://doi.org/10.1016/j.jenvrad.2018.03.006>.
- 1303 Iakovleva, V. S., & Ryzhakova, N. K. (2003). A method for estimating the convective
1304 radon transport velocity in soils. *Radiation Measurements*, *36*, 389–391.
1305 [https://doi.org/10.1016/S1350-4487\(03\)00157-4](https://doi.org/10.1016/S1350-4487(03)00157-4).

- 1306 Ishihara, Y., Shimojima, E., & Harada, H. (1992). Water vapor transfer beneath bare soil
 1307 where evaporation is influenced by a turbulent surface wind. *Journal of Hydrology*,
 1308 *131*(1–4), 63–104. [https://doi.org/10.1016/0022-1694\(92\)90213-F](https://doi.org/10.1016/0022-1694(92)90213-F).
- 1309 Jackson, R. D. (1973). Diurnal changes in soil water content during drying. In R. R.
 1310 Bruce (Ed.), *Field soil water regime* (pp. 37–55). Madison, Wisconsin USA: Soil
 1311 Science Society of America, Inc. <https://doi.org/10.2136/sssaspecpub5.c3>.
- 1312 Jackson, T. J., O’Neill, P., & Swift, C. T. (1997). Passive microwave observation of
 1313 diurnal surface soil moisture. *IEEE Transactions in Geoscience and Remote*
 1314 *Sensing*, *35*, 1210–1222. <https://doi.org/10.1109/36.628788>.
- 1315 Jury, W., & Horton, R. (2004). *Soil physics*. (6th ed.). Hoboken, NJ, USA: John Wiley &
 1316 Sons, Inc. (ISBN: 0-471-05965-X)
- 1317 Kadalbajoo, M. K., & Awasthi, A. (2006). A numerical method based on Crank-Nicolson
 1318 scheme for Burgers equation. *Applied Mathematics and Computation*, *182*(2),
 1319 1430–1442. <https://doi.org/10.1016/j.amc.2006.05.030>.
- 1320 Kidder, R. E. (1957). Unsteady flow of gas through a semi-infinite porous medium.
 1321 *Journal of Applied Mechanics*, *24*, 329–332. <https://doi.org/10.1115/1.4011542>.
- 1322 Kimball, B. A. (1983). Canopy gas exchange: Gas exchange with soil. In H. M. Taylor,
 1323 W. R. Jordan, & T. R. Sinclair (Eds.), *Limitations to efficient water use in crop*
 1324 *production* (pp. 215–226). Madison, Wisconsin USA: ASA, CSSA, and SSSA.
 1325 <https://doi.org/10.2134/1983.limitationstoefficientwateruse.c14>.
- 1326 Koch, S. E., & Siedlarz, L. M. (1999). Mesoscale gravity waves and their environment in
 1327 the central United States during STORM-FEST. *Monthly Weather Review*, *127*(12),
 1328 2854–2879. [https://doi.org/10.1175/1520-0493\(1999\)127<2854:MGWATE>2.0.CO;2](https://doi.org/10.1175/1520-0493(1999)127<2854:MGWATE>2.0.CO;2).
- 1329 Kochina, N. N. (1961). Observations of nonlinear waves on an atmospheric inversion.
 1330 *Journal of Applied Mathematics and Mechanics*, *25*(6), 1597–1607.
 1331 [https://doi.org/10.1016/0021-8928\(62\)90138-7](https://doi.org/10.1016/0021-8928(62)90138-7).
- 1332 Koppel, L. L., Bosart, L. F., & Keyser, D. (2000). A 25-yr climatology of large-amplitude
 1333 hourly surface pressure changes over the conterminous United States. *Monthly*
 1334 *weather review*, *128*(1), 51–68.
 1335 [https://doi.org/10.1175/1520-0493\(2000\)128<0051:AYCOLA>2.0.CO;2](https://doi.org/10.1175/1520-0493(2000)128<0051:AYCOLA>2.0.CO;2).
- 1336 Kraichnan, R. H. (1956). Pressure fluctuations in turbulent flow over a flat plate. *The*
 1337 *Journal of The Acoustical Society of America*, *28*(3), 378–390.
 1338 <https://doi.org/10.1121/1.1908336>.
- 1339 Kuang, X., Jiao, J. J., & Li, H. (2013). Review on airflow in unsaturated zones induced
 1340 by natural forcings. *Water Resources Research*, *49*, 6137–6165.
 1341 <https://doi.org/10.1002/wrcr.20416>.
- 1342 Kurganov, A. (2016). Central schemes: A powerful black-box solver for nonlinear
 1343 hyperbolic PDEs. In R. Abgrall & C.-W. Shu (Eds.), *Handbook of Numerical*
 1344 *Analysis* (pp. 525–548). 1000 AE Amsterdam, The Netherlands: Elsevier B.V.
 1345 <https://doi.org/10.1016/bs.hna.2016.09.008>.
- 1346 Kurt, A., Çenesiz, Y., & Tasbozan, O. (2015). On the solution of Burgers Equation with
 1347 the new fractional derivative. *Open Physics*, *13*(1), 355–360.
 1348 <https://doi.org/10.1515/phys-2015-0045>.
- 1349 Laemmel, T., Mohr, M., Schack-Kirchner, H., Schindler, D., & Maier, M. (2017). Direct
 1350 observation of wind-induced pressure-pumping on gas transport in soil. *Soil Science*
 1351 *Society of America Journal*, *81*, 770–774.
 1352 <https://doi.org/10.2136/sssaj2017.01.0034n>.
- 1353 Lebeau, M., & Konrad, J.-M. (2009). Natural convection of compressible and
 1354 incompressible gases in undeformable porous media under cold climate. *Computers*
 1355 *and Geotechnics*, *36*, 435–445. <https://doi.org/10.1016/j.compgeo.2008.04.005>.
- 1356 Leventhall, G. (2007). What is infrasound? *Progress in Biophysics and Molecular Biology*,
 1357 *93*(1–3), 130–137. <https://doi.org/10.1016/j.pbiomolbio.2006.07.006>.
- 1358 Lewicki, J. L., Evans, W. C., Hillel, G. E., Sorey, M. L., Rogie, J. D., & Brantley, S. L.
 1359 (2003). Shallow soil CO₂ flow along the San Andreas and Calaveras Faults,
 1360 California. *Journal of Geophysical Research*, *108*(B4), 2187.

- 1361 <https://doi.org/10.1029/2002JB002141>.
- 1362 Li, J., You, K., Zhan, H., & Huang, G. (2012). Analytical solution to subsurface air
1363 pressure in a three-layer unsaturated zone with atmospheric pressure changes.
1364 *Transport in Porous Media*, *93*, 461–474. <https://doi.org/10.1007/s11242-012-9964-5>.
- 1365 Li, J., Zhan, H., & Huang, G. (2011). Applicability of the linearized governing equation of
1366 gas flow in porous media. *Transport in Porous Media*, *87*, 815–834.
1367 <https://doi.org/10.1007/s11242-011-9720-2>.
- 1368 Li, Y., & Smith, R. B. (2010). Observation and theory of the diurnal continental thermal
1369 tide. *Journal of The Atmospheric Sciences*, *76*(9), 2752–2765.
1370 <https://doi.org/10.1175/2010JAS3384.1>.
- 1371 Luce, C. H., Tonina, D., Gariglio, F., & Applebee, R. (2013). Solutions for the diurnally
1372 forced advection-diffusion equation to estimate bulk fluid velocity and diffusivity in
1373 streambeds from temperature time series. *Water Resources Research*, *49*, 488–506.
1374 <https://doi.org/10.1029/2012WR012380>.
- 1375 Maier, M., Schack-Kirchner, H., Aubinet, M., Goffi, S., Longdoz, B., & Parent, F. (2012).
1376 Turbulence effect on gas transport in three contrasting forest soils. *Soil Science*
1377 *Society of America Journal*, *76*, 1518–1528. <https://doi.org/10.2136/sssaj2011.0376>.
- 1378 Marlton, G., Charlton-Perez, A., Harrison, G., & Lee, C. (2019). Calculating atmospheric
1379 gravity wave parameters from infrasound measurements. In A. Le Pichon, E. Blanc,
1380 & A. Hauchecorne (Eds.), *Infrasound Monitoring for Atmospheric Studies*. (pp.
1381 701–719). Gewerbestrasse 11, 6330 Cham, Switzerland: Springer Nature Switzerland
1382 AG. https://doi.org/10.1007/978-3-319-75140-5_22.
- 1383 Marty, J., Ponceau, D., & Dalaudier, F. (2010). Using the international monitoring
1384 system infrasound network to study gravity waves. *Geophysical Research Letters*,
1385 *37*(19), L19802. <https://doi.org/10.1029/2010GL044181>.
- 1386 Mass, C. F., Steenburgh, W. J., & Schultz, D. M. (1991). Diurnal surface-pressure
1387 variations over the continental United States and the influence of sea level reduction.
1388 *Monthly Weather Review*, *119*(12), 2814–2830.
1389 [https://doi.org/10.1175/1520-0493\(1991\)119<2814:DSPVOT>2.0.CO;2](https://doi.org/10.1175/1520-0493(1991)119<2814:DSPVOT>2.0.CO;2).
- 1390 Massman, W. J., Berryman, E., & Frank, J. (2021). *Pressure pumping dramatically*
1391 *impacts soil and snowpack CO₂ fluxes and profiles*. AmeriFlux video postcard at
1392 <https://ameriflux.lbl.gov/>, then follow the link [https://ameriflux.lbl.gov/pressure-](https://ameriflux.lbl.gov/pressure-pumping-dramatically-impacts-soil-and-snowpack-co2-fluxes-and-profiles/)
1393 [pumping-dramatically-impacts-soil-and-snowpack-co2-fluxes-and-profiles/](https://ameriflux.lbl.gov/pressure-pumping-dramatically-impacts-soil-and-snowpack-co2-fluxes-and-profiles/).
- 1394
- 1395 Massman, W. J., Frank, J. M., & Mooney, S. J. (2010). Advancing investigation and
1396 modeling of first-order fire effects on soils. *Fire Ecology*, *6*, 36–54.
1397 <https://doi.org/10.4996/fireecology.0601036>.
- 1398 Massman, W. J., & Lee, X. (2002). Eddy covariance flux corrections and uncertainties in
1399 long-term studies of carbon and energy exchanges. *Agricultural and Forest*
1400 *Meteorology*, *113*(1–4), 121–144. <https://doi.org/10.1029/2000WR900128>.
- 1401 Massman, W. J., Sommerfeld, R., Mosier, A. R., Zeller, K. F., Hehn, T., & Rochelle, S.
1402 (1997). A model investigation of turbulence-driven pressure pumping effects on the
1403 rate of diffusion of CO₂, N₂O and CH₄ through layered snowpacks. *Journal of*
1404 *Geophysical Research*, *102*, 18,851–18,863. <https://doi.org/10.1029/97JD00844>.
- 1405 Massmann, J., & Ferrier, D. F. (1992). Effects of atmospheric pressures on gas transport
1406 in the vadose zone. *Water Resources Research*, *28*(3), 777–791.
1407 <https://doi.org/10.1029/91WR02766>.
- 1408 Massmann, J. W. (1989). Applying groundwater flow models in vapor extraction system
1409 design. *Journal of Environmental Engineering*, *115*, 129–149.
1410 [https://doi.org/10.1061/\(ASCE\)0733-9372\(1989\)115:1\(129\)](https://doi.org/10.1061/(ASCE)0733-9372(1989)115:1(129)).
- 1411 Mohamed, N. A. (2019). Solving one- and two-dimensional unsteady Burgers’ equation
1412 using fully implicit finite difference schemes. *Arab Journal of Basic and Applied*
1413 *Sciences*, *26*(1), 254–268. <https://doi.org/10.1080/25765299.2019.1613746>.
- 1414 Moya, M. R., Sánchez-Cañete, E. P., Vargas, R., López-Ballesteros, A., Oyonarte, C.,
1415 Kowalski, A. S., et al. (2019). CO₂ dynamics are strongly influenced by low

- 1416 frequency atmospheric pressure changes in semiarid grasslands. *Journal of*
 1417 *Geophysical Research: Biogeosciences*, *124*, 902–917.
 1418 <https://doi.org/10.1029/2018JG004961>.
- 1419 Muskat, M. (1937). *The flow of homogeneous fluids through porous media*. New York,
 1420 NY, USA: McGraw-Hill Book Co., Inc. (ISBN-13: 978-0934634168)
- 1421 Nachshon, U., Dragila, M., & Weisbrod, N. (2012). From atmospheric winds to fracture
 1422 ventilation: Cause and effect. *Journal of Geophysical Research: Biogeosciences*,
 1423 *117*(G2), G02016. <https://doi.org/10.1029/2011JG001898>.
- 1424 Nield, D. A. (1982). Onset of convection in a porous layer saturated by an ideal gas.
 1425 *International Journal of Heat and Mass Transfer*, *25*(10), 1605–1606.
 1426 [https://doi.org/10.1016/0017-9310\(82\)90039-4](https://doi.org/10.1016/0017-9310(82)90039-4).
- 1427 Nieveen, J. P., El-Kilani, R. M. M., & Jacobs, A. F. G. (2001). Behaviour of the static
 1428 pressure around a tussock grassland/forest interface. *Agricultural and Forest*
 1429 *Meteorology*, *106*(4), 253–259. [https://doi.org/10.1016/S0168-1923\(00\)00234-3](https://doi.org/10.1016/S0168-1923(00)00234-3).
- 1430 Novak, M. D. (2016). Importance of soil heating, liquid water loss, and vapor flow
 1431 enhancement for evaporation. *Water Resources Research*, *52*, 8023–8038.
 1432 <https://doi.org/10.1002/2016WR01884>.
- 1433 Or, D., & Wraith, J. M. (2000). Comment on ‘On water vapor transport in field soils’ by
 1434 Anthony T. Cahill and Marc B. Parlange. *Water Resources Research*, *36*,
 1435 3103–3105. <https://doi.org/10.1029/2000WR900124>.
- 1436 Ostendorf, D. W., Hinlein, E. S., Lutenecker, A. J., & Kelley, S. P. (2000). Soil gas
 1437 transport above a jet fuel/solvent spill at Plattsburgh Air Force Base. *Water*
 1438 *Resources Research*, *36*(9), 2531–2547. <https://doi.org/10.1029/2000WR900128>.
- 1439 Parlange, M. B., Cahill, A. T., Nielsen, D. R., Hopmans, J. W., & Wendroth, O. (1998).
 1440 Review of heat and water movement in field soils. *Soil & Tillage Research*, *47*, 5–10.
 1441 [https://doi.org/10.1016/S0167-1987\(98\)00066-X](https://doi.org/10.1016/S0167-1987(98)00066-X).
- 1442 Phillips, O. M. (1991). *Flow and reactions in permeable rocks*. New York, NY, USA:
 1443 Cambridge University Press. (ISBN-13: 978-0521380980, ISBN-10: 0521380987)
- 1444 Platzman, G. W. (1964). An exact integral of complete spectral equations for unsteady
 1445 one-dimensional flow. *Tellus*, *16*(4), 422–431.
 1446 <https://doi.org/10.3402/tellusa.v16i4.8995>.
- 1447 Press, W. H., Teukolsky, S. A., Vetterling, W. T., & Flannery, B. P. (2007). *Numerical*
 1448 *recipes*. (Third ed.). Cambridge, U.K.: Cambridge University Press. (ISBN
 1449 978-0-521-88068-8)
- 1450 Rains, F. A., Stoy, P. C., Welch, C. M., Montagne, C., & McGlynn, B. L. (2016). A
 1451 comparison of methods reveals that enhanced diffusion helps explain cold-season soil
 1452 CO₂ efflux in a lodgepole pine ecosystem. *Cold Regions Science and Technology*,
 1453 *121*, 16–24. <https://doi.org/10.1029/WR025i010p02159>.
- 1454 Ralph, F. M., Neiman, P. J., & Keller, T. L. (1999). Deep-tropospheric gravity waves
 1455 created by leeside cold fronts. *Journal of the Atmospheric Sciences*, *56*(17),
 1456 2986–3009.
 1457 [https://doi.org/10.1175/1520-0469\(1999\)056<2986:DTGWCB>2.0.CO;2](https://doi.org/10.1175/1520-0469(1999)056<2986:DTGWCB>2.0.CO;2).
- 1458 Raspert, R., Abbott, J.-P., Webster, J., Yu, J., Talmadge, C., Alberts, K., et al. (2019).
 1459 New systems for wind noise reduction for infrasonic measurements. In A. Le Pichon,
 1460 E. Blanc, & A. Hauchecorne (Eds.), *Infrasound Monitoring for Atmospheric Studies*.
 1461 (pp. 91–124). Gewerbestrasse 11, 6330 Cham, Switzerland: Springer Nature
 1462 Switzerland AG. https://doi.org/10.1007/978-3-319-75140-5_3.
- 1463 Reicosky, D. C., Gesch, R. W., Wagner, S. W., Gilbert, R. A., Wente, C. D., & Morris,
 1464 D. R. (2008). Tillage and wind effects on soil CO₂ concentrations in muck soils. *Soil*
 1465 *& Tillage Research*, *99*, 221–231. <https://doi.org/10.1016/j.still.2008.02.006>.
- 1466 Robinson, A. L., Sextro, R. G., & Fisk, W. J. (1997). Soil-gas entry into an experimental
 1467 basement driven by atmospheric pressure fluctuations – measurements, spectral
 1468 analysis, and model comparison. *Atmospheric Environment*, *31*, 1477–1485.
 1469 [https://doi.org/10.1016/S1352-2310\(96\)00304-4](https://doi.org/10.1016/S1352-2310(96)00304-4).

- 1470 Rose, C. W. (1968). Water transport in soil with a daily temperature wave I. theory and
 1471 experiment. *Australian Journal of Soil Research*, 6, 31–44.
 1472 <https://doi.org/10.1071/SR9680031>.
- 1473 Ruppert, J. H., & Bosart, L. F. (2014). A case study of the interaction of a mesoscale
 1474 gravity wave with a mesoscale convective system. *Monthly Weather Review*, 142(4),
 1475 1403–1429. <https://doi.org/10.1175/MWR-D-13-00274.1>.
- 1476 Rutten, M. M. (2015). *Moisture in the topsoil from large-scale observations to small-scale*
 1477 *process understanding*. Unpublished master’s thesis, Delft University of Technology.
 1478 (ISBN: 978-94-6186-434-5)
- 1479 Sanders, F., & Gyakum, J. R. (1980). Synoptic–Dynamic climatology of the “Bomb”.
 1480 *Monthly Weather Review*, 108(10), 1589–1606.
 1481 [https://doi.org/10.1175/1520-0493\(1980\)108<1589:SDCOT>2.0.CO;2](https://doi.org/10.1175/1520-0493(1980)108<1589:SDCOT>2.0.CO;2).
- 1482 Scanlon, B. R., Nicot, J. P., & Massmann, J. W. (2002). Soil gas movement in
 1483 unsaturated systems. In A. W. Warrick (Ed.), *Soil physics companion* (pp.
 1484 297–341). Boca Raton, FL 33431: CRC Press LLC.
 1485 <https://doi.org/10.1201/9781420041651.ch8>.
- 1486 Scotter, D. R., & Raats, P. A. C. (1969). Dispersion of water vapor in soil due to
 1487 turbulence. *Soil Science*, 108(3), 170–176.
- 1488 Scotter, D. R., Thurtell, G. W., & Raats, P. A. C. (1967). Note: Dispersion resulting
 1489 from sinusoidal gas flow in porous materials. *Soil Science*, 104(4), 206–308.
- 1490 Shan, C. (1995). Analytical solutions for determining vertical air permeability in
 1491 unsaturated soils. *Water Resources Research*, 31(9), 2193–2200.
 1492 <https://doi.org/10.1029/95WR01653>.
- 1493 Shaw, R. H., Paw U, K. T., Zhang, X. J., Gao, W., den Hartog, G., & Neumann, H. H.
 1494 (1990). Retrieval of turbulent pressure fluctuations at the ground surface beneath a
 1495 forest. *Boundary-Layer Meteorology*, 50(3), 319–338.
 1496 <https://doi.org/10.1007/BF00120528>.
- 1497 Shreffler, J. H., & Binkowski, F. S. (1981). Observations of pressure jump lines in the
 1498 Midwest, 10–12 August 1976. *Monthly Weather Review*, 109(8), 1713–1725.
 1499 [https://doi.org/10.1175/1520-0493\(1981\)109<1713:OOPJLI>2.0.CO;2](https://doi.org/10.1175/1520-0493(1981)109<1713:OOPJLI>2.0.CO;2).
- 1500 Shurpali, N. J., Verma, S. B., Clement, R. J., & Billesbach, D. P. (1993). Seasonal
 1501 distribution of methane flux in a Minnesota peatland measured by eddy correlation.
 1502 *Journal of Geophysical Research - Atmospheres*, 98(D11), 20649–20655.
 1503 <https://doi.org/10.1029/93JD02181>.
- 1504 Sommerfeld, R. A., & Rocchio, J. E. (1993). Permeability measurements on new and
 1505 equitemperature snow. *Water Resources Research*, 29(8), 2485–2490.
 1506 <https://doi.org/10.1029/93WR01071>.
- 1507 Thomas, J. W. (1995). *Numerical partial differential equations*. New York, NY, USA:
 1508 Springer-Verlag. (ISBN 978-0-387-97999-1)
- 1509 Todd-Brown, K. E. O., Hopkins, F. M., Kivlin, S. N., Talbot, J. M., & Allison, S. D.
 1510 (2012). A framework for representing microbial decomposition in coupled climate
 1511 models. *Biogeochemistry*, 109(1), 19–33. <https://doi.org/10.1007/s10533-011-9635-6>.
- 1512 Waddington, E. D., Cunningham, J., & Harder, S. L. (1995). The effects of snow
 1513 ventilation on chemical concentrations. In E. W. Wolff & R. C. Bales (Eds.),
 1514 *Chemical exchange between the atmosphere and polar snow* (pp. 403–451). Berlin
 1515 Heidelberg: Springer-Verlag. https://doi.org/10.1007/978-3-642-61171-1_18.
- 1516 Wang, H., & Takle, E. S. (1995). A numerical simulation of boundary-layer flows near
 1517 shelterbelts. *Boundary-Layer Meteorology*, 75(1-2), 141–173.
 1518 [https://doi.org/10.1016/0883-2927\(94\)90052-3](https://doi.org/10.1016/0883-2927(94)90052-3).
- 1519 Wang, X., Lei, H., Feng, L., Zhu, J., Li, Z., & Jiang, Z. (2020). Analysis of the
 1520 characteristics of gravity waves during a local rainstorm event in Foshan, China.
 1521 *Atmospheric and Oceanic Science Letters*, 13(2), 163–170.
 1522 <https://doi.org/10.1080/16742834.2020.1719567>.
- 1523 Weisbrod, N., Dragila, M. I., Nachshon, U., & Pillersdorf, M. (2009). Falling through the
 1524 cracks: The role of fractures in Earth-atmosphere gas exchange. *Geophysical*

- 1525 *Research Letters*, 36(2), L02401. <https://doi.org/10.1029/2008GL036096>.
- 1526 Xu, L., Lin, X., Amen, J., Welding, K., & McDermitt, D. (2014). Impact of changes in
1527 barometric pressure on landfill methane emission. *Global Biogeochemical Cycles*, 28,
1528 79–95. <https://doi.org/10.1002/2013GB004571>.
- 1529 Yu, J., Raspet, R., Webster, J., & Abbott, J. (2011). Wind noise measured at the ground
1530 surface. *The Journal of The Acoustical Society of America*, 129(2), 622–632.
1531 <https://doi.org/10.1121/1.3531809>.